JOURNAL OF GEOPHYSICAL RESEARCH, VOL. 116, F03007, doi:10.1029/2010JF001749, 2011

Initial stages of erosion and bed form development in a turbulent flow around a cylindrical pier

Cristian Escauriaza[1] and Fotis Sotiropoulos[2]

Received 22 April 2010; revised 24 March 2011; accepted 3 May 2011; published 30 July 2011.

[1] Bed load transport and erosion in fine sediment beds are mainly driven by the dynamics of the near-bed turbulent flow. In situations when the shear stress is not sufficiently high to produce significant transport, the presence of an obstacle can initiate erosion and trigger the development of bed forms, which are produced by the emergence of the turbulent horseshoe vortex (THV) system. We develop a numerical model to investigate the initial stages of erosion and the development of ripples produced by the THV system in the vicinity of a surface-mounted cylindrical pier. The flow is simulated using the detached eddy simulation approach, which has been shown to accurately resolve most of the turbulent stresses produced by the THV. To compute the erosion, the Exner equation is coupled to a new bed load transport model that directly incorporates the effect of the instantaneous flow field on sediment transport. The morphodynamic model is integrated simultaneously with the flow equations using an arbitrary Lagrangian-Eulerian method for moving boundaries. Even though the time rate of scour is slower compared to the observations, the computed results exhibit essentially all the dynamics of erosion, including the emergence of ripples reported in the experiments of Dargahi (1990). The bed forms show similar velocities as reported in the experiments and are shown to be statistically similar to ripples measured in laboratory experiments and in nature. To our knowledge, this is the first three-dimensional simulation to capture the ripple dynamics that evolve naturally from the nonlinear interactions between the flow and the bed.

Citation: Escauriaza, C., and F. Sotiropoulos (2011), Initial stages of erosion and bed form development in a turbulent flow around a cylindrical pier, *J. Geophys. Res.*, *116*, F03007, doi:10.1029/2010JF001749.

1. Introduction

[2] The development and dynamics of bed forms in turbulent flows over mobile beds have been the subject of extensive research since the pioneering work of *Exner* [1920, 1925]. Complex interactions and feedbacks between the turbulent flow and the sediment bed give rise to these organized dynamic sedimentary patterns at the interface. In general, bed forms exhibit a remarkable dynamics and a wide range of time and length scales, with multiple structures traveling at different speeds, and merging events that give shape to the interface between water and sediment. In addition, erosion and deposition processes and the role of bed forms as roughness elements can have great relevance in engineering flows and in applications to river and aquatic habitat restoration projects.

[3] Bed forms classified as ripples are small structures produced by the turbulent fluctuations generated near the bed. They commonly exist in fine sediment beds and have no interaction with the free surface [*Allen*, 1966; *Kennedy*, 1969]. The physical mechanisms that give rise to these bed forms, however, are not entirely clear, even though many recent investigations have yielded new insights into the relation between the turbulent flow and the initial development of ripples [see, e.g., *Best*, 1992; *Coleman and Melville*, 1996; *Venditti et al.*, 2005, 2006].

[4] The origin of small bed forms was first studied using linear stability analysis for an erodible bed subject to a unidirectional steady flow, analyzing the growth of perturbations on the bed surface [e.g., *Kennedy*, 1969; *Engelund and Fredsøe*, 1982]. Experimental investigations have established that there is an intimate relation between the development of ripples and the velocity fluctuations and bursts produced by near-wall unsteady coherent vortices in the turbulent boundary layer. The initial bed instability reported by *Best* [1992] was linked to the hairpin vortices in the turbulent boundary layer over smooth beds, and in particular to the sweep events that seem to generate small accumulations of sediment which grow and propagate downstream. *Coleman and Melville* [1996] showed that this initial bed instability grows as a regular pattern of short-wavelength and small-amplitude sediment waves that evolve into ripples as time progresses. *Raudkivi* [1997] also connected the origin of ripples to velocity bursts near the bed, and observed that they travel at different speeds depending on

[1]Departamento de Ingeniería Hidráulica y Ambiental, Pontificia Universidad Católica de Chile, Santiago, Chile.
[2]St. Anthony Falls Laboratory, Department of Civil Engineering, University of Minnesota, Minneapolis, Minnesota, USA.

0148-0227/11/2010JF001749

their height. As pointed out by *Raudkivi* [1997], the bed self-organizes after the initial ripples go through a sequence of bed form merging events, as smaller ripples present higher displacement velocities while larger structures become slower and more stable.

[5] In the recent study by *Venditti et al.* [2006], two principal mechanisms were identified as responsible for the initial development of transverse ripples on the bed. They seem to arise either by a Kelvin-Helmholtz type of instability of the entire interface or as a consequence of small bed defects that can be produced by the turbulent flow. In particular, *Venditti et al.* [2006] discussed the effects that obstacles might have on the flow. The flow field around flow obstructions creates bed disturbances capable of propagating downstream and forming ripples in fine sediment beds.

[6] Many questions still remain on the origin of bed forms and the most important features of the flow that control their dynamics. The complexity of bed form initiation mechanisms and the variability in their height, amplitude and velocity of propagation have motivated the development of several models to simulate ripple dynamics. From models based on simple discrete formulations in one or two dimensions [e.g., *Niño et al.*, 2002], to methodologies that also include simplified deterministic or stochastic equations that describe the bed surface evolution based on approximations of the Exner equation [see *Jerolmack and Mohrig*, 2005; *McElroy and Mohrig*, 2009]. To the best of our knowledge, however, no realistic bed forms have been obtained from 3-D simulations of the coupled bed dynamics and unsteady turbulent flows.

[7] The recent computational investigations of flows past surface-mounted obstacles mounted on fixed beds at high Reynolds numbers, carried out using coherent-structure resolving statistical turbulence models [*Paik et al.*, 2007, 2009; *Escauriaza and Sotiropoulos*, 2011a], provide test bed flow fields that can be employed to investigate the relation between unsteady vortical structures in turbulent flows, sediment transport, and bed dynamics. In particular, these numerical simulations using the detached eddy simulation (DES) approach [*Spalart et al.*, 1997; *Spalart*, 2009] have successfully resolved the complex dynamics of the turbulent horseshoe vortex (THV) system around surface-mounted obstacles and explained the physical mechanisms that give rise to the bimodal velocity probability density functions (pdfs) observed in experiments [*Devenport and Simpson*, 1990; *Simpson*, 2001]. Furthermore, these simulations have clearly shown that the DES approach is capable of resolving essentially all turbulence scales produced by the fluctuations of the THV in the junction region that corresponds to the union between the bed and the obstacle, and the associated increase in the turbulence kinetic energy (TKE) and turbulence production in front of the obstacle.

[8] In this paper we build on the work of *Paik et al.* [2007] and *Escauriaza and Sotiropoulos* [2011a] to develop a novel numerical model for simulating bed erosion processes past a cylindrical pier mounted on a mobile fine-sand bed. We consider bed scour under clear-water conditions, that is, the incoming boundary layer cannot initiate sediment motion and the unsteadiness of the THV is the main mechanism responsible for the bed load transport, local erosion, and bed form development. Focusing on clear-water scour driven by large-scale coherent vortices induced by the cylindrical pier enables us to use the aforementioned numerical simulations of *Escauriaza and Sotiropoulos* [2011a] as starting point for this work, with the computational domain and discretization shown in Figure 1. An important point to emphasize in this regard is that because most turbulence in the vicinity of the pier is produced by large-scale, low-frequency fluctuations of the THV, essentially all turbulence scales that are responsible for transport in the region where scour originates can be resolved efficiently and at realistic Reynolds numbers using the DES approach. Therefore, we can focus in this work on developing a bed load transport model that directly incorporates the effect of the resolved near-bed, fluctuating hydrodynamic forces on sediment transport. The proposed bed load transport model is based on the vectorial formulation of *Kovacs and Parker* [1994] and its main novelty lies on the approach adopted to calculate the bed load flux. Rather than calculating the sediment velocity in the bed load layer by correlating it to the flow velocity near the bed using extrapolation or other approximate approaches (as done in essentially all available numerical models of sediment transport [e.g., *Ushijima*, 1996; *Roulund et al.*, 2005]), we develop and solve a momentum equation governing the instantaneous velocity of sediment grains inspired by our recent Lagrangian model of bed load transport [*Escauriaza and Sotiropoulos*, 2011b]. The instantaneous hydrodynamic forces appearing in the right hand side of sediment momentum equation (lift, drag, etc.) are calculated using the near-bed instantaneous resolved flow, thus providing a straightforward approach for incorporating near-bed turbulent fluctuations into the bed load transport model.

[9] The specific test case we simulate is the flow past a circular cylinder mounted on the mobile bed of a rectangular channel at Re = 39,000, which corresponds to the case studied experimentally by *Dargahi* [1989, 1990]. This case is selected because *Dargahi* [1989, 1990] visualized and described for the first time the unsteady characteristics of the vortices in the junction region for both flat and mobile beds, and reported the development and displacement of ripples formed by the legs of the THV system during the initial stages of erosion starting from a flat bed for the first 735 s. It is important to note that the objective of our work is not to predict equilibrium scour but rather to understand the effects of large-scale unsteady vortices on bed erosion and ripple dynamics in high Reynolds number turbulent flows.

[10] The paper is organized as follows. In section 2 we provide a brief description of the physics of the THV that develops around a surface-mounted cylinder in a rectangular channel at Reynolds number Re = 39,000 [*Dargahi*, 1989] and explain the dynamics of the flow as emerged from the simulations of *Escauriaza and Sotiropoulos* [2011a]. The development of the coupled model of flow and bed erosion, the governing equations and the numerical methods employed in this investigation are explained in section 3. In section 4 we report the results of the simulation, which captures the initial dynamics of erosion produced by the THV, and we also compare the numerical results with the experimental observations of *Dargahi* [1990]. To study the bed form dynamics, in this section we also explore the statistical characteristics of the ripples that are induced by the legs of the THV system at the sides of the cylinder. The

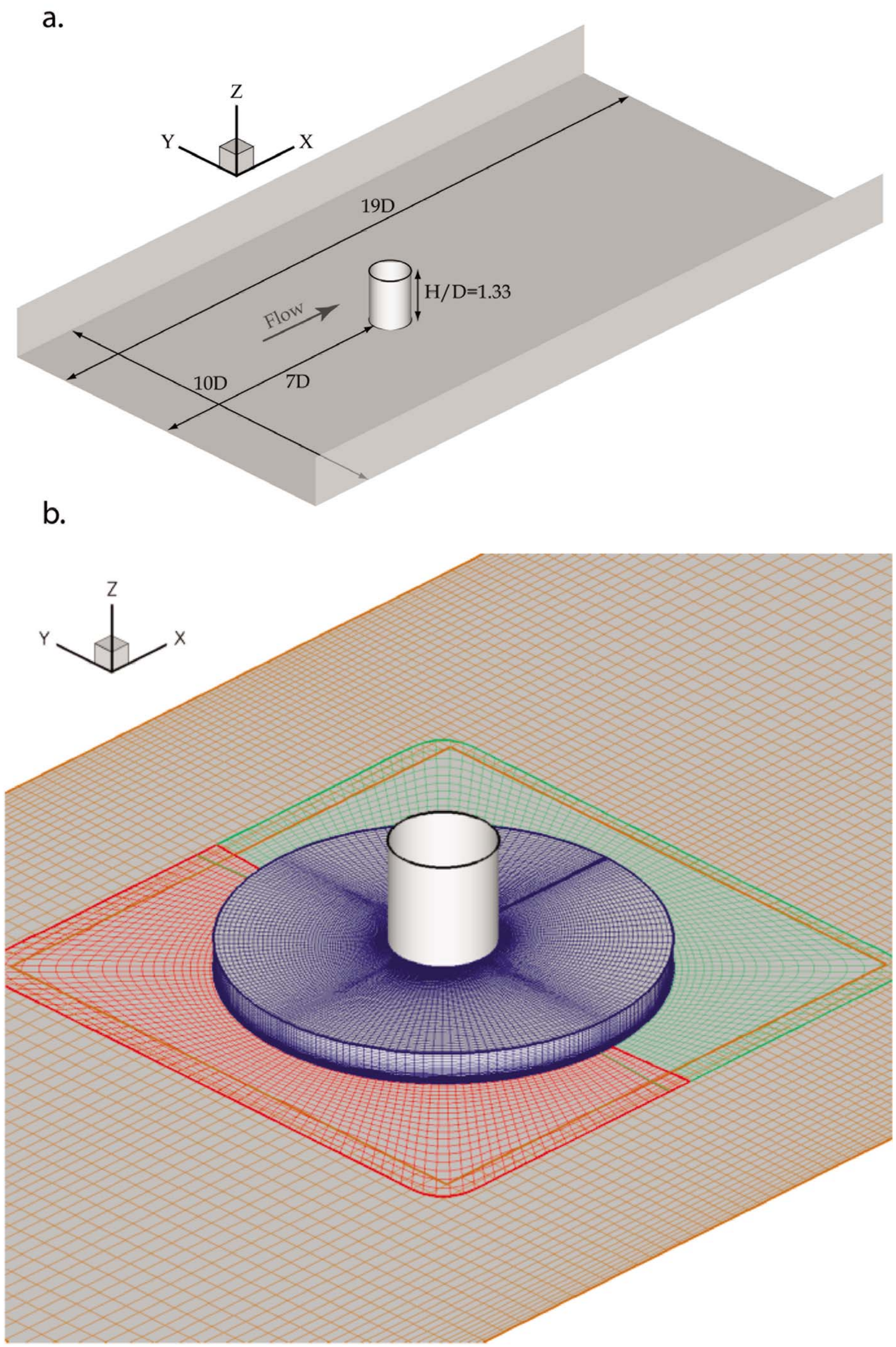

Figure 1. Geometry of the computational domain. (a) Section of the channel considered in the DES simulations of *Escauriaza and Sotiropoulos* [2011a]; (b) details of the overset grid layout with a total of 3.0 million grid nodes, 70% around the cylinder.

conclusions in section 5 summarize the findings of the present investigation and outline topics for future research.

2. Previous Work on Turbulent Flows Past Surface-Mounted Obstacles

2.1. The Dynamics of the Turbulent Horseshoe Vortex on a Flat Fixed Bed

[11] A surface-mounted obstacle in a turbulent boundary layer induces adverse pressure gradients, causing the formation of the dynamically-rich THV system in the junction of the obstacle with the wall. In their pioneering work, *Devenport and Simpson* [1990] studied in detail the structure of the THV at $Re = 1.15 \times 10^5$ in the vicinity of the leading edge of a cylindrical wing-shaped pier and described its dynamics by analyzing their experimental measurements at the plane of symmetry. Their results showed that the THV is characterized by low-frequency oscillations that produce bimodal probability density functions (pdfs) of the horizontal and vertical velocities close to the wall at the sym-

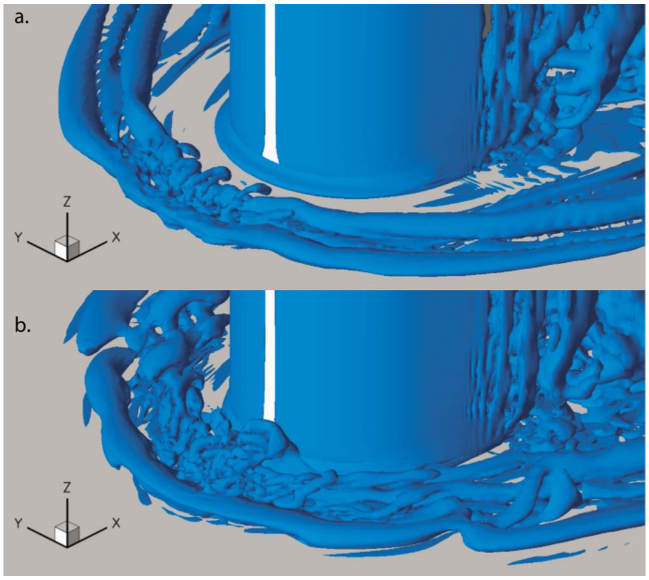

Figure 2. (a and b) Visualization of the 3-D instantaneous coherent structures in the turbulent flow past a surface-mounted cylinder at Re = 39,000 computed by *Escauriaza and Sotiropoulos* [2011a], using the q criterion proposed by *Hunt et al.* [1988]. The incoming flow direction coincides with the positive X axis, and the instantaneous images are separated by 0.8 s.

metry plane in front of the cylinder. The THV dynamics was attributed to the existence of two dynamic states corresponding to the *backflow mode*, in which the return flow of the THV generates a wall jet that penetrates upstream of the obstacle, and the *zero-flow mode* that occurs when the near-wall flow cannot penetrate upstream and it is ejected vertically upwards. The aperiodic interplay between these two modes produces high turbulent stresses in the THV region that are at least one order of magnitude larger than in the approaching turbulent boundary layer [*Escauriaza and Sotiropoulos*, 2011a].

[12] *Paik et al.* [2007] were the first to reproduce numerically and explain the physical mechanisms governing the rich dynamics of the THV as documented in Devenport and Simpson's experiments. Comparisons between the calculated solutions with DES and the experiments [*Devenport and Simpson*, 1990] showed that the model can reproduce the bimodal pdfs of velocity fluctuations and the pocket of large TKE in the upstream junction of the pier with the bed. Additionally, *Paik et al.* [2007] showed that the interplay between the backflow and zero-flow modes was a consequence of the development of small-scale hairpin vortices near the wall that destroyed the main THV and produced strong ejections of wall fluid, increasing the shear stress at the wall as also observed in previous experiments [*Doligalski et al.*, 1994].

[13] *Dargahi* [1989] studied the flow around a cylindrical pier mounted on the bed of a rectangular channel and performed flow visualizations that showed multiple vortices shedding quasiperiodically from the separation point upstream of the cylinder. A qualitative description of the flow dynamics at the symmetry plane revealed a complex sequence of vortex formation and merging, with at least five vortices that interact in front of the cylinder.

[14] Using the same numerical model presented by *Paik et al.* [2007], *Escauriaza and Sotiropoulos* [2011a] simulated the flow past the cylinder, for the same experimental configuration studied by *Dargahi* [1989] at Re = 20,000 and 39,000, to investigate the effect of the Reynolds number on the THV dynamics. The simulations reproduced the experimental observations with good accuracy (see *Escauriaza and Sotiropoulos* [2011a] for details). Similar results have also been obtained by large-eddy simulation (LES) of flows past cylindrical piers albeit at lower Reynolds numbers [*Kirkil et al.*, 2008].

[15] Figure 2 depicts 3-D instantaneous q isosurfaces [*Hunt et al.*, 1988] to visualize the coherent dynamics of the computed flow around the cylinder [*Escauriaza and Sotiropoulos*, 2011a]. Figure 2 illustrates clearly the basic instability mechanism, which is associated with the aperiodic emergence of hairpin vortices that destabilize the primary vortex and give rise to the bimodal velocity pdfs. For more details the reader is referred to extensive discussion by *Paik et al.* [2007] and *Escauriaza and Sotiropoulos* [2011a].

[16] The quasiperiodic dynamics of the energetic THV system illustrated in Figure 2, showing instantaneous q isosurfaces separated by 0.8 s, is also responsible for the instantaneous shear stress increments at the bed. Figure 3 shows contours of nondimensional friction velocity u_τ at the bed for the same instant in time depicted in Figure 2b. Bands of high shear stress appear at the position of the THV legs and multiple pockets of concentrated stresses are produced during the development of the THV instability. The wall vorticity ejected vertically is accompanied with the entrainment of high-speed fluid that produces regions of high shear velocity for short periods of time, which are comparable to the magnitude of u_τ at the cylinder sides as shown in Figure 3a. The waviness of the vortex seen in the 3-D visualizations with q isosurfaces is reflected on the shear stress distribution at the legs of the THV. The time series of u_τ at the symmetry plane plotted in Figure 3b clearly show the intensity and large variability of the instantaneous shear velocity produced by the THV dynamics.

2.2. Lagrangian Dynamics of Bed Load Transport

[17] The DES of *Escauriaza and Sotiropoulos* [2011a] motivated the development of a Lagrangian particle model [*Escauriaza and Sotiropoulos*, 2011b] to investigate the effects of the THV system on entrainment and transport of fine sand grains. The purpose of this study was not to predict scour but rather to give fundamental insights into the initiation of motion and particle dynamics transported by coherent structures. The Lagrangian model of *Escauriaza and Sotiropoulos* [2011b] inspired the new bed load transport model that will subsequently be presented in this paper and for that it is important to review the modeling framework and key findings of that study.

[18] The model of *Escauriaza and Sotiropoulos* [2011b] considered a one-way coupling approach, integrating the trajectory and momentum equation for individual sediment particles. Multiple hydrodynamic forces acting on each particle are computed by tracking the location of the particle within the Eulerian grid, and interpolating the velocity and pressure fields to the particle position. Considering drag,

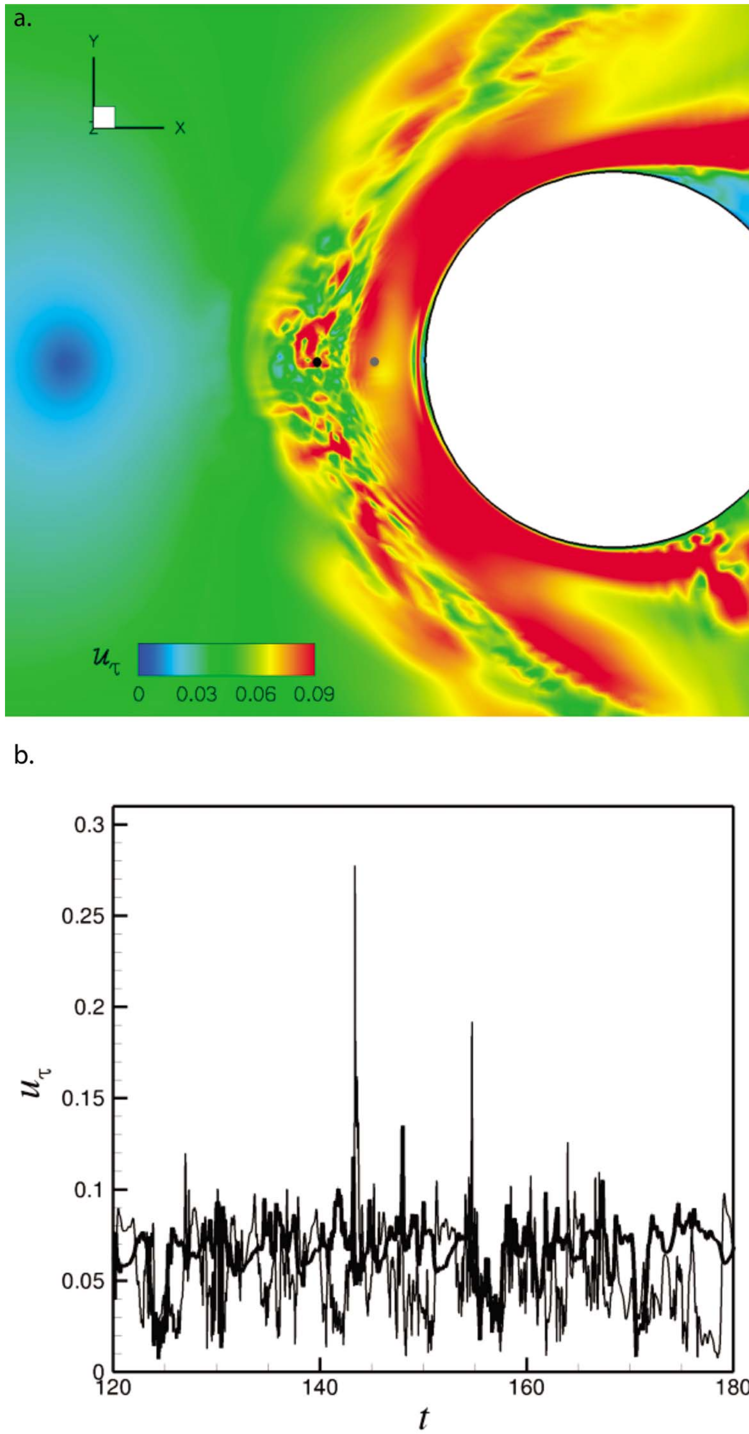

Figure 3. (a) Contours of instantaneous nondimensional shear velocity distribution u_τ, showing the pockets of high u_τ produced by the THV instability [*Escauriaza and Sotiropoulos*, 2011a] at the same instant shown in Figure 2b. (b) Time series of nondimensional shear velocity at two points on the symmetry plane plotted in thick and fine lines corresponding to the gray and black points marked in Figure 3a, respectively. The fluctuations produced by the THV dynamics increase the instantaneous magnitude of u_τ by more than 6 times.

gravity, lift, added mass, pressure, and viscous forces, the complete momentum equation per unit mass for the grain velocity v_i can be written in tensor notation, using also the expression for the particle specific gravity $SG = \rho_s/\rho$ (SG = 2.65 for sand), in the following nondimensionalized expression:

$$\frac{dv_i}{dt} = \frac{1}{(SG + C_m)}\left[\frac{1}{St}v_{ri} - \frac{\delta_{i3}}{Fr^2} + C_L\left(\epsilon_{ijk}v_{rj}\omega_k\right) + (1 + C_m)\frac{Du_i}{Dt}\right] \quad (1)$$

where the relative particle velocity in the cartesian framework is defined as $v_{ri} = u_i - v_i$, δ_{ij} is Kronecker's delta and ϵ_{ijk} is the tensorial permutation symbol to determine the vector perpendicular to the relative velocity v_{ri} and vorticity ω_i fields in the lift term [*Auton et al.*, 1988]. All the variables are nondimensionalized with the bulk velocity of the flow ($\mathcal{U}$ = 0.26 m/s), and the length scale equal to the cylinder diameter (D = 0.15 m). The various dimensionless parameters that appear in the particle momentum equation (1) are defined as follows. The Stokes number, defined as the ratio between the particle response time determined from the drag force and the characteristic time scale of the flow, can be expressed as follows:

$$St = \frac{4}{3}\frac{d}{C_D|\mathbf{v}_r|} \quad (2)$$

where C_D is the drag coefficient for sand [*Engelund and Hansen*, 1967], which is a function of the particle Reynolds number, and the relative velocity magnitude $|\mathbf{v}_r|$ and the particle diameter d are nondimensionalized by the characteristic velocity and length scales of the flow. For the present case the median size of sediment grains corresponds to a nondimensional particle diameter of d = 0.0024 [*Dargahi*, 1990], which yields $St \ll 1$. Consequently, the energetic large-scale flow structures have a significant role on transport [*Crowe et al.*, 1998; *Escauriaza and Sotiropoulos*, 2009]. The Froude number Fr, in equation (1) is defined as follows:

$$Fr = \frac{\mathcal{U}}{\sqrt{(SG - 1)gD}} \quad (3)$$

where $\mathcal{U}$ is the bulk velocity of the flow and D the cylinder diameter. Finally, C_L and C_m in equation (1) are the nondimensional lift and added mass coefficients [*Auton et al.*, 1988]. For more details on the various terms in equation (1) and all other aspects of the Lagrangian model the reader is referred to *Escauriaza and Sotiropoulos* [2011b].

[19] *Escauriaza and Sotiropoulos* [2011b] carried out simulations of particles located in the region influenced by the unsteadiness of the THV system by placing up to 10^5 sediment grains at repose on top of the flat bed in front of the cylinder. The simulations showed that the interaction of the vortices with the wall is the fundamental mechanism that increases the instantaneous bed shear stress and produces transport. The aperiodic dynamics of the resolved flow field of the THV system increases the instantaneous forces acting on the particles and initiates episodic and highly intermittent motion of sediment grains by saltation and sliding along the bed, features that are known to characterize bed load transport near the threshold of motion [e.g., *Ancey et al.*, 2006]. Another important physical process that was captured by the Lagrangian model was the formation of streaks of particles on the bed, which are aligned with the low shear stress regions between counterrotating vortices (see *Escauriaza and Sotiropoulos* [2011b] for details). This finding is also in good agreement with experimental observations in similar conditions [see *Kaftori et al.*, 1995].

[20] In addition, sediment ejections and transverse accumulation of particles were found to always occur at the location of the legs of the THV system. Phase-space plots of calculated instantaneous flow velocities reported by *Escauriaza and Sotiropoulos* [2011b] at the location where sediment ejections occur showed that vertical and streamwise velocity fluctuations near the bed at approximately 40° from the symmetry plane show frequent events of positive streamwise and vertical velocities (outward excursions), generally followed by strong events of downward flow in sweep-like events. These two types of events coincide with particle entrainment in this region, as reported by *Escauriaza and Sotiropoulos* [2011b], and their predominance is the consequence of the strong vertical flow associated with the intertwining counterrotating vorticity of the THV legs. Wall vortices lift near-wall fluid and produce strong vertical velocities and a posterior inrush of high-velocity fluid near the bed. *Nelson et al.* [1995] observed in their experiments that events of the turbulent velocity fluctuations corresponding to ejections and sweeps coincide with an increase of the sediment transport flux. Similar events have been identified by *Best* [1992] as potential conditions for creating sediment bed perturbations and forming ripples.

[21] *Escauriaza and Sotiropoulos* [2011b] also quantified and characterized the statistics of the bed load flux in their simulations by studying the time series of transport behind the cylinder. The high degree of intermittency with multiple episodes of transport of different magnitudes separated by hiatuses of arbitrary duration, yielded a sediment flux characterized by the fractal curve known as the devil's staircase. In addition, the sediment transport events showed to give rise to a multifractal sediment flux. The multifractality of the sediment transport induced by the dynamically rich THV system was demonstrated rigorously by calculating the multifractal or singularity spectrum of the sediment flux.

[22] In summary, the main conclusion from the Lagrangian simulations of *Escauriaza and Sotiropoulos* [2011b] is that the aperiodic dynamics of the THV give rise to Lagrangian dynamics of sediment grains in the bed load layer that closely resemble what has been observed in laboratory experiments. In what follows we employ the DES approach for simulating the flow along with key ideas from the Lagrangian model of *Escauriaza and Sotiropoulos* [2011b] to develop a novel model for predicting bed erosion and bed form evolution.

3. Computational Model

[23] In this section we present the governing equations for the flow field and sediment transport and the numerical methods employed to solve these equations.

3.1. Governing Equations

3.1.1. Resolved Flow Equations

[24] The governing equations for the resolved flow are the 3-D unsteady Reynolds-averaged continuity and Navier-

Stokes equations nondimensionalized using the cylinder diameter D and the bulk velocity $\mathcal{U}$ as characteristic length and velocity scales, respectively. The equations are transformed to a generalized curvilinear system to compute the flow field in complex domains and moving boundaries. For the time-accurate simulations of turbulent flows and sediment transport with mobile beds, the arbitrary Lagrangian-Eulerian (ALE) formulation [*Hirt et al.*, 1974] is implemented to incorporate the dynamic deformation of the computational domain that arises from the bed erosion as explained in the next section. The governing equations in the ALE form can be written in vector format and in strong conservation form as follows:

$$\Gamma \frac{\partial Q}{\partial t} + J \frac{\partial}{\partial \xi^j}\left(F^j - F^j_v\right) = Jh \tag{4}$$

where

$$\Gamma = \mathrm{diag}[0\,1\,1\,1]$$
$$Q = [P, u_1, u_2, u_3]^T$$
$$F^j = \frac{1}{J}\Big[U^j, u_1\left(U^j - U^j_0\right) + P\xi^j_{x_1}, u_2\left(U^j - U^j_0\right) + P\xi^j_{x_2}, u_3\left(U^j - U^j_0\right) + P\xi^j_{x_3}\Big]^T$$
$$F^j_v = \frac{1}{J}\left(\frac{1}{Re} + \nu_t\right)\left[0, g^{mj}\frac{\partial u_1}{\partial \xi^m} + R_{m1}\xi^j_{x_m}, g^{mj}\frac{\partial u_2}{\partial \xi^m} + R_{m2}\xi^j_{x_m}, g^{mj}\frac{\partial u_3}{\partial \xi^m} + R_{m3}\xi^j_{x_m}\right]^T$$
$$h = \frac{1}{J}\left[0, u_1\frac{\partial U^j_0}{\partial \xi^j}, u_2\frac{\partial U^j_0}{\partial \xi^j}, u_3\frac{\partial U^j_0}{\partial \xi^j}\right]^T$$

In these equations $P = p + \frac{2}{3}k$, where k is the turbulence kinetic energy and p is the pressure divided by the density, u_i (i = 1, 2, 3) are the Cartesian velocity components, x_i are the Cartesian coordinates, J is the Jacobian of the curvilinear coordinate transformation, $\xi^j_{x_i}$ are the metrics of the transformation, U^j are the contravariant velocity components $U^j = u_i\xi^i_{x_j}$, g^{ij} are the components of the contravariant metric tensor $g^{ij} = \xi^i_{x_k}\xi^j_{x_k}$, Re is the Reynolds number, ν_t is the eddy viscosity, and the tensor R_{ij} is defined as: $R_{ij} = \frac{\partial u_i}{\partial \xi^k}\xi^k_{x_j}$. The source vector h on the right hand side of equation (4) is incorporated to account for the effects of the moving grid (due to the continuous bed deformation) on the flow field [*Ahn and Kallinderis*, 2006]. The vector h and the advective flux contain the contravariant components of the Lagrangian grid velocity U^j_0, defined in terms of the cartesian Lagrangian velocity of the moving grid $\dot{x}_i$, as: $U^j_0 = \dot{x}_i\xi^j_{x_i}$ The Reynolds number is defined as: $Re = \mathcal{U}D/\nu$ where ν is the kinematic viscosity of the fluid. Local geometric conservation conditions for moving grids and global mass conservation for the entire computational domain are ensured at all times (see *Escauriaza* [2008] for details).

3.1.2. Turbulence Model

[25] For the turbulence model we employ the DES approach [*Spalart et al.*, 1997; *Spalart*, 2009], which is a hybrid URANS/LES formulation based on the one-equation eddy-viscosity model of *Spalart and Allmaras* [1994, hereinafter S-A]. The model can be expressed in the moving (ALE) curvilinear coordinate system as follows:

$$\frac{\partial \tilde{\nu}}{\partial t} + J\frac{\partial}{\partial \xi^j}\left[F^j_t - F^j_{tv}\right] + JH_t + Jh_t = 0 \tag{5}$$

where

$$F^j_t = \frac{1}{J}\left[\left(U^j - U^j_0\right)\tilde{\nu}\right]$$
$$F^j_{tv} = \frac{1}{J}\left[\frac{1}{\sigma}\left(\frac{1}{Re} + \tilde{\nu}\right)g^{mj}\frac{\partial \tilde{\nu}}{\partial \xi^m}\right]$$
$$H_t = \frac{1}{J}\left[-c_{b_1}(1 - f_{t_2})\tilde{S}\tilde{\nu} + \left(c_{w_1}f_w - \frac{c_{b_1}}{\kappa^2}f_{t_2}\right)\left(\frac{\tilde{\nu}}{d_w}\right)^2 - \frac{1}{\sigma}c_{b_2}g^{mj} \cdot \frac{\partial \tilde{\nu}}{\partial \xi^m}\frac{\partial \tilde{\nu}}{\partial \xi^m}\right]$$
$$h_t = \frac{1}{J}\tilde{\nu}\frac{\partial U^j_0}{\partial \xi^j}$$

The working variable $\tilde{\nu}$ in the S-A turbulence model has a direct relation to the eddy viscosity, ν_t, and the destruction term contains the length scale d_w, which is defined as the distance from solid walls. For a detailed explanation of the variables and functions that appear in the turbulence model equation (5), the reader is referred to *Paik et al.* [2007].

[26] The DES approach is such that the S-A turbulence model in equation (5) functions in URANS mode near solid boundaries while switches to perform the role of the subgrid scale (SGS) model in the large-eddy simulation (LES) regions away from the wall, where the grid density is sufficient to resolve the energetic scales of fluid motion (for details see *Spalart et al.* [1997] and *Spalart* [2009]). In the present investigation the method does require a specific modification to predict correctly the eddy viscosity near the wall as discussed extensively by *Paik et al.* [2007] and *Escauriaza and Sotiropoulos* [2011a].

3.1.3. Sediment and Bed Model

[27] In this section we describe a novel sediment transport model for fine sand that is capable of incorporating the instantaneous information provided by the DES of the THV system past the bed-mounted cylinder studied experimentally by *Dargahi* [1990] and computationally by *Escauriaza and Sotiropoulos* [2011a, 2011b].

[28] A complete Eulerian model of sediment transport can be derived from the conservation of momentum for the two phases (water and sediment) [see *Drew*, 1983; *Lakehal*, 2002; *Hsu et al.*, 2004]. For the cylindrical pier flow studied in this research, we simplify the sediment model assuming that there is only bed load transport in a layer of constant thickness and local uniform concentration above the bed, which is assumed as equal to $3d_{90}$ based on the experiments of *van Rijn* [1984] for fine sand with similar diameters. This vertically integrated approach reduces considerably the computational cost of the coupled simulation, using instantaneous quantities to predict transport in nonequilibrium conditions.

[29] Our model is based on the vectorial approach of *Kovacs and Parker* [1994] and *Parker et al.* [2003] for determining the bed load flux coupled with a new equation for calculating the instantaneous sediment velocity within the bed load layer. The sediment flux vector, which is used as input

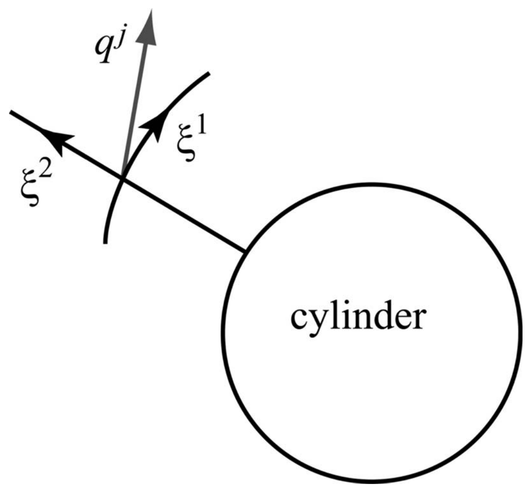

Figure 4. Schematic depiction of the bed load flux vector at every grid node in the 2-D curvilinear bed coordinate system around the surface-mounted cylinder [ξ^1, ξ^2]. Sediment transport and the elevation of the bed are computed in a two-dimensional plane. The ξ^3 coordinate direction is perpendicular to it and coincides with the vertical direction in the Cartesian system.

in the Exner equation (see equation (12) below), is calculated as the product between the bed-areal concentration γ, which indicates the sediment volume per unit of area that contributes to transport, and the sediment velocity vector in the bed load layer. The equation of the bed load flux can thus be written in tensor notation (j = 1, 2), as follows:

$$q^j = \gamma V^j \tag{6}$$

As the ξ^3 axis of the generalized curvilinear system coincides with the vertical direction in the computational mesh, the flux components q^j in equation (6) correspond to the contravariant components of the bed load flux referred to the two-dimensional coordinate system [ξ^1, ξ^2], as shown in Figure 4, where V^j (j = 1, 2) are the contravariant components of sediment velocity. In what follows, we first discuss in detail the model we propose for calculating V^j followed by the approach we adopt for computing γ. Subsequently we present the Exner equation and outline the complete bed load transport model.

3.1.3.1. The Sediment Velocity Equation

[30] The key idea we put forth in this paper is to compute the instantaneous (albeit vertically integrated) sediment velocity in the bed load layer by solving the momentum equation of the particles, equation (1), used in the Lagrangian model of *Escauriaza and Sotiropoulos* [2011b] but transformed to the Eulerian framework attached to the bed and considering instantaneous forces computed from the resolved DES flow field. This new approach not only increases the level of physical realism of the sediment transport dynamics but also provides a consistent way for computing the unsteady bed load flux in cases when near-wall coherent structures become the main mechanism of sediment transport.

[31] The equation utilized to compute the velocity of the sediment in the unsteady bed load Eulerian model is directly derived from the Lagrangian particle model of *Escauriaza and Sotiropoulos* [2011b]. *Anderson and Jackson* [1967] performed the formal derivation of the Eulerian momentum equation from the Lagrangian model to describe the flow in fluidized beds. The governing equations in the Eulerian framework are based on local spatial averages of particle velocities. This description is only valid if the instantaneous velocities are assumed to be decomposed in two separate scales, for which the unsteady local spatial average values are resolved and the fluctuation contributions are considered separately. This concept, known as double-averaging technique, has been developed and extensively studied by *Nikora et al.* [2007]. For the Exner equation, *Coleman and Nikora* [2009] have recently derived a general form including the spatial averaging for a scale smaller than the sediment grains. This formulation is ideally suited to incorporate in future research the effects of spatial scales that are averaged over the bed discretization when the grid size becomes larger than the sediment diameter (see related discussion in section 5).

[32] The vertically integrated momentum equation for the sediment velocity inside the bed load layer is considered as a two-dimensional equation in the curvilinear coordinate system given by [ξ^1, ξ^2]. To facilitate the description of generalized bed deformations, the Eulerian momentum equation (see equation (7) below) is fully transformed to the curvilinear 2-D system attached to the bed; that is, the balance momentum is carried out along the bed-conforming curvilinear directions. According to the full transformation approach, the components of the sediment velocities and forces are transformed in the generalized curvilinear coordinate system using contravariant components V^m, with m = 1, 2, as previously presented in equation (6). The contravariant velocities are the components of the total resolved sediment velocity in the direction of the nonorthogonal coordinates of the curvilinear system (ξ^1 and ξ^2).

[33] Therefore, the fully transformed momentum equation used to compute the sediment velocity, assuming a locally uniform bed-areal concentration γ, is expressed as follows (m = 1, 2):

$$\frac{\partial}{\partial t} V^m + V^k \frac{\partial V^m}{\partial \xi^k} + V^k V^r \Gamma^m_{rk} = F^m \tag{7}$$

where V^m and F^m are the contravariant components of the sediment velocity and integrated forces in the [ξ^1, ξ^2] coordinate system, and the bed is represented by a surface of constant ξ^3 (perpendicular to the projection shown in Figure 4). The full coordinate transformation to the nonorthogonal curvilinear system in equation (7) include the terms Γ^m_{rk}, which are the Christoffel symbols of the second kind from the covariant derivative operator [*Aris*, 1962]. The term F^m contains the second-order vertical integration of the particle forces that appear on the right hand side of equation (1) defined in the Eulerian framework, which are computed as follows:

$$F^m = \int_b^{b+\delta_b} \left(f_i \, \xi^m_{x_i} \right) d\xi^3 \approx \frac{\delta_b}{2} \left[\left(f_i \, \xi^m_{x_i} \right) \Big|_{b+\delta_b} + \left(f_i \, \xi^m_{x_i} \right) \Big|_b \right] \tag{8}$$

where b is the bed elevation, δ_b is the bed load layer thickness, f_i are the cartesian components of the hydrodynamic forces, and $\xi^m_{x_i}$ are the metrics of the coordinate transformation. For additional information of the full derivation of the model, the reader is referred to *Escauriaza* [2008].

[34] The novelty of equation (7) lies in the fact that it provides a physics-based framework for incorporating directly the effects of the instantaneous fluctuations of the hydrodynamic forces produced by the turbulent flow on the bed load flux. Equation (7) represents a significant departure from most RANS-based models of sediment transport in nonequilibrium conditions available in the literature, which use an approximation of the flow friction velocity u_τ, calculated from wall functions or from the flow velocity near the edge of the bed load layer, to predict the instantaneous bed load flux using empirical formulas calibrated for equilibrium conditions [*Ushijima*, 1996; *Roulund et al.*, 2005].

[35] It is worth noting that this new formulation for computing the bed load flux given by equations (6) and (7) employs the same assumptions of the Lagrangian particle model of *Escauriaza and Sotiropoulos* [2011b] given by equation (1): it does not consider the unresolved scales of motion (SGS contributions) and neglects higher-order correlations that appear from averaging locally instantaneous quantities in the balance of momentum as it is derived by *Anderson and Jackson* [1967]. These simplifying assumptions can be justified by the fact that our emphasis is on sediment transport near the threshold of motion as already discussed above.

3.1.3.2. The Local Areal Concentration Model

[36] To complete the calculation of the instantaneous bed load flux (see equation (6)), we also need an approach for calculating the local areal concentration γ. A major difficulty in this regard stems from the fact that no expressions for the areal concentration exist in the literature for the nonequilibrium conditions that exist for bed load transport upstream of wall-mounted obstacles as the experiment of *Dargahi* [1990] we consider in this work. The Lagrangian simulations of *Escauriaza and Sotiropoulos* [2011b], however, do suggest that there is a close relationship between the instantaneous shear stress magnitude and grain motion in the THV region. This observation motivates the use of an empirical formula for the bed areal concentration that is a function of the shear stress. Since no relations exist today in the literature linking the instantaneous bed areal concentration to instantaneous flow quantities at the bed, we utilize in equation (6) an equilibrium empirical formula for the time-averaged γ that is a function of the time-averaged shear stress. The key assumption we thus make is that empirical formulas for γ linking its time-averaged local value to the time-averaged local value of the bed shear stress also hold true when the values for γ and shear stress are replaced with their respective local instantaneous values. Obviously there is no physical basis for this assumption but it is one that is dictated by the aforementioned lack of quantitative bed load experiments emphasizing instantaneous quantities. This modeling limitation not withstanding, the model we propose herein is general and can be readily extended to incorporate a more physics-based model for the bed-areal concentration. Such undertaking is beyond the scope of the present work and shall await future more sophisticated experiments.

[37] The formula for the bed areal concentration we employ in our model is computed from the relation for the percentage of moving particles per unit area of *Engelund and Fredsøe* [1976], which was also employed in the scour simulations of *Roulund et al.* [2005]. *Engelund and Fredsøe* [1976] introduced an expression for the probability of a particle moving on the bed p_{ef} computed as function of the shear stress as follows,

$$p_{ef} = \left[1 + \left(\frac{\pi\mu_d/6}{\tau_* - \tau_{*c}}\right)^4\right]^{-1/4} \tag{9}$$

where μ_d is the dynamic friction coefficient, τ_* the nondimensional shear stress or Shields number, and for the critical nondimensional shear stress τ_{*c}, we implement the correction used by *Roulund et al.* [2005] in beds with arbitrary slope, which is expressed as follows,

$$\tau_{*c} = \tau_{*c_0}\left[\cos\beta\left(1 - \frac{\sin^2\alpha\ \tan^2\beta}{\mu_s^2}\right)^{1/2} - \frac{\cos\alpha\ \sin\beta}{\mu_s}\right] \tag{10}$$

where τ_{*c_0} is the critical Shields parameter for horizontal beds, μ_s is the static friction coefficient, α is the angle between the local flow velocity and the direction of maximum steepness, and β is the angle of local bed inclination with respect to a horizontal plane [see *Roulund et al.*, 2005].

[38] Assuming that the fine sand particles can be represented by spheres, we compute the areal concentration γ using p_{ef} and the number of particles per unit area [see *Roulund et al.*, 2005]. Thus, the final expression for γ is given as follows:

$$\gamma = \frac{1}{6}\pi d^3 \frac{p_{ef}}{d^2} \tag{11}$$

where p_{ef} is given by equation (9) and d is the sediment grain diameter.

3.1.3.3. The Exner Equation

[39] To determine the instantaneous bed elevation, we employ the sediment mass balance at the bed or Exner equation, whose generalized form has been given by *Paola and Voller* [2005]. Through this equation, we determine the volume of sediment that is eroded or deposited as a function of the instantaneous bed load flux. The conservation of mass for an element of the bed in the [ξ^1, ξ^2] curvilinear coordinate system can be expressed as follows:

$$\frac{\partial b}{\partial t} = \frac{-1}{(1-\lambda_p)}\left[\frac{\partial \gamma}{\partial t} + J\frac{\partial}{\partial \xi^j}\left(\frac{q^j}{J}\right)\right] \tag{12}$$

where b is the bed elevation, λ_p is the porosity that is assumed as constant and equal to 0.35, γ is calculated from equation (11), and the bed load flux is computed from the following equation:

$$q^j = \frac{1}{6}\pi d^3 \frac{p_{ef}}{d^2} V^j = \gamma\ V^j \tag{13}$$

where V^j is calculated by solving the sediment momentum equations (7).

[40] The evolution of the bed topography is determined from the solution of the Exner equation considering the additional restriction imposed to the bed elevation, since the local slope cannot exceed the maximum angle of repose of the sediment. To incorporate the avalanches of sediment that are produced when the bed slope exceeds the angle of repose, we include in the solution the physically-based mass conservation approach implemented by *Marieu et al.* [2008] to

account for local avalanches, which showed good results in simulations of ripple evolution. During the iterations of the numerical calculation of the Exner equation, the local slope is computed for each grid node at the bed. If the bed inclination is steeper than the angle of repose, the local bed slope is instantaneously corrected, such that the maximum angle of repose is enforced at every grid point. The elevation of the surrounding nodes is iteratively modified by extrapolating linearly the slope equal to the maximum angle of repose, preserving the total mass on the bed (see *Marieu et al.* [2008] for more details).

[41] Summarizing, the model we propose herein constitutes a new approach for simulating bed load transport and erosion driven by large-scale coherent structures resolved by the DES simulation. The governing equations of the flow field are coupled to a bed load transport and morphodynamic model that directly incorporates the effects of instantaneous fluctuations of the resolved velocity and pressure fields. In turn, the dynamics of the erosion and deposition processes that modify the computational domain are considered in the computation of the turbulent junction flow. The details of the numerical algorithms we employ to solve the governing equations for the flow and sediment models are discussed in the following sections.

3.2. Numerical Algorithms

[42] The computational domain is discretized by using overset grid decomposition techniques as explained by *Paik et al.* [2007]. The model includes moving boundary interface methods to determine the deformation produced by bed erosion and deposition in a coupled manner with the solution of the flow equations. Here we employ the ALE formulation [*Hirt et al.*, 1974] as discussed in the governing equations section. The time integration of the governing equations is carried out by adopting a time stepping artificial compressibility method [*Paik et al.*, 2007], enhanced with local time stepping and V-cycle multigrid acceleration and modified to be adapted to the present ALE framework (see *Escauriaza* [2008] for details).

[43] The equations that comprise the unsteady bed load and erosion model, equations (7) and (12), are solved numerically in conjunction with the flow equations to couple the flow field with the evolution of the bed. To integrate the sediment equations simultaneously with the solution of the Navier-Stokes equation, the relation given by equation (7) is discretized using a pseudo-time iteration algorithm, with a second-order backward time difference, and implicit treatment of the space derivative and Christoffel terms. The iterations to determine the sediment velocity are coupled with the bed model, equation (12). For every pseudo-time iteration, the local critical shear stress τ_{*c} is obtained with the partial bed elevation at the pseudo-time iteration using the relation explained by *Roulund et al.* [2005] for arbitrary bed slopes, and the bed areal concentration given in the equation (9) is computed using the currently available instantaneous sediment velocity.

[44] After calculating the bed load flux from the areal concentration and the sediment velocity, as expressed in equation (13), we solve and update the bed elevation from the Exner equation (12). A dual-time stepping four-stage Runge-Kutta algorithm is employed to advance the bed elevation b in pseudo-time. The spatial derivatives of the bed load flux in equation (12) are discretized using first-order upwinding to ensure that the bed surface remains smooth at all times. The time derivatives in equation (12) are discretized with a three-point-backward, Euler-implicit temporal-integration scheme. As mentioned in the previous section, the local slope is checked in every Runge-Kutta iteration, and it is modified using the algorithm proposed by *Marieu et al.* [2008].

3.3. Computational Details

[45] We simulate the flow past a vertical circular cylinder mounted at the bottom of a rectangular open channel using the same discretization of *Escauriaza and Sotiropoulos* [2011a] shown in Figure 1b, with an overset grid layout and a total of 3.0×10^6 grid nodes. This configuration was studied experimentally by *Dargahi* [1989, 1990] who carried out flow visualization experiments and reported measurements for Re = 39,000. In the experiments the cylinder diameter was $D = 0.15$ m and it was mounted at the center of a flume with width B = 1.5 m (10D) and water depth of H = 0.2 m (1.33D). The cylinder was placed at a distance of 18.0 m (120D) from the inlet of the channel and consequently the flow approaching the cylinder can be considered as fully-developed turbulent open channel flow. The bed was composed by uniform sand with median diameter d_{50} = 0.36 mm, which is hydraulically smooth with a k_s^+ value of 4.3. A no-slip boundary condition is applied to solid walls, and given the low Froude number of the experiments (Fr = 0.18) the free surface is considered as a symmetric boundary condition, which has shown to be appropriate for this flow (see *Escauriaza and Sotiropoulos* [2011a] for details).

[46] As discussed by *Escauriaza and Sotiropoulos* [2011a], the computations for this mesh exhibited all major flow features observed in the original experiments of *Dargahi* [1989] for flat beds. In the present simulations we study the flow and initial evolution of erosion around the cylinder for Re = 39,000, starting from the flat bed condition and a snapshot of the statistically converged flow field solution obtained in our previous flat, rigid bed investigation [*Escauriaza and Sotiropoulos*, 2011a, 2011b].

4. Development of Erosion and Bed Forms

[47] In this section, the results of the simulations are compared with the experimental observations of *Dargahi* [1990] for an erodible bed. *Dargahi* [1990] mostly provided a qualitative analysis of the initial erosion process produced by the unsteady coherent vortices of the THV system, giving a description of the initial stages of erosion around the cylinder for the first 735 s. He also reported additional data for the long-term characteristics of erosion and the development of bed forms during the scour process.

4.1. Erosion in Front of the Cylinder

[48] For the initial development of erosion, *Dargahi* [1990] reported multiple features of the bed related to the dynamics of the THV system that are also captured by our simulations: (1) development of two depressions on the bed at the symmetry plane during the initial stages of erosion, which later merge into a single scour hole in front of the cylinder; (2) maximum erosion occurred always at the base of the cylinder, at approximately ±45° from the symmetry

plane; (3) time series of scour depth showed quasiperiodic oscillations connected to the time scales of vortex shedding in the THV system; and (4) bed forms emerged at the sides of the cylinder along the legs of the THV.

[49] Figure 5 shows the simulated scouring process in 2-D plots of bed elevation at the plane of symmetry corresponding to t = 5, 40, 95, and 735 s, where the zero bed elevation corresponds to the initial flat bed position and the coordinate origin is located at the center of the cylinder. It is important to note that the initial flow conditions for the simulations differ from the experiments, which start from zero velocity and require a time interval to establish the statistically stationary turbulent flow at Re = 39,000. The symmetry plane bed profiles, however, show very similar features to the experimental trends. During the first 5 s, the symmetry plane remains mostly flat, except for the accumulation of sediment located at $X = -0.8$, as seen in Figure 5a. After 40 s, two clear depressions shown in Figure 5b start to appear in front of the cylinder, with minimum values at around $X = -0.55$ and $X = -0.7$. The location with higher elevation in Figure 5a at $X = -0.8$ now has an approximately zero elevation. At 95 s the two depressions persist, with the increase of the upstream depression and the formation of a mound with the maximum around $X = -0.86$. The bed profile at 735 s shown in Figure 5d has only one depression in front of the cylinder, which is consistent with the growth of a single scour hole that develops at the leading edge of the cylinder as reported by *Dargahi* [1990].

[50] Therefore, the evolution of the bed elevation at the symmetry plane shown in Figure 5 follows the same patterns described by *Dargahi* [1990]. For all the 2-D bed profiles we observe that the scoured region is extended for less than one cylinder diameter upstream, and a part of the material transported by the return flow of the THV system is accumulated at the interface between the active and immobile zones, heaping the bed surface.

[51] To have a better understanding of the mechanisms that generate the simulated bed profiles at the symmetry plane, it is worth exploring the flow field characteristics in this region in tandem with the bed elevation patterns. Figure 6 depicts representative finite-time average velocities (obtained by averaging the resolved velocity field over 5 s intervals) for two time windows that show the flow field at which the bed has been subjected during the erosion process. The two plots shown in Figures 6a and 6b depict the average velocity vectors colored by spanwise vorticity, illustrating the characteristics of the averaged flow field for two of the cases discussed in Figure 5. These plots show similar characteristics for all the 5 s averages computed from our solution. In a previous section we provided evidence about the significant increase of the turbulent stresses near the bed associated with the complex and highly dynamic interaction of the THV system and the wall. Recall that the THV dynamics gave rise to the extraction of positive vorticity tongues from the wall and bimodal dynamics of velocity fluctuations at the symmetry plane, which were linked with large-scale instabilities causing the growth of hairpin vortices between the vortex and the wall that wrapped around and disorganized the THV system. For the finite-time averaged flow fields in Figure 6 we observe that in both cases there is a characteristic vortical structure located in the region where the upstreambed depression develops. It is important to note that the accumulation of sediment at the bed behind the depression in this zone also coincides with the outer turn of the vortex, which is the region where the zero-flow mode of the THV system emerges.

[52] Turning now our attention to the time evolution of erosion, the bed at the symmetry plane exhibits regions with different dynamics. In some regions there is a steady scouring of the bed, that is, the bed descends smoothly at all times during the erosion process. Other regions of the bed, on the other hand, present significant variations of elevation during scouring as the bed is continuously eroded but the elevation time series exhibit intense oscillations that are connected with the rich THV dynamics [*Dargahi*, 1990]. The scour depth time series for the first 800 s, plotted in Figure 7, shows the rate at which the bed is eroded at two points where the two trends occur along with the evolution of the maximum scour depth over the entire bed d_{max}. The nonequilibrium conditions determine the rapid initial erosion at the two points in the THV region and the maximum scour depth on the entire bed. The maximum erosion coincides with the observations of *Dargahi* [1990] as it always occurs at the sides of the cylinder at approximately ±45° from the plane of symmetry, which also coincides with the region where the shear stress has the largest magnitude (see subsequent discussion). The deepening of the bed occurs continuously and smoothly at points of the bed closer to the cylinder, as seen in the point $X = -0.54$. A particular characteristic observed at the upstream point on the symmetry plane, at $X = -0.66$, is the periodicity of the bed elevation, which occurs due to the generation of small sediment waves in the return flow of the THV. This fluctuating region of the bed reaches the transition region separating the active erosion in the vicinity of the cylinder, from the low shear stress zone with no mobility. Therefore, the simulations also reproduce the quasiperiodicity on the time series of erosion reported by *Dargahi* [1990], with characteristic frequencies of f = 0.10 Hz and f = 0.19 Hz (or periods T = 10 s and T = 5.26 s respectively), which are similar to the timescales of the THV system dynamics extracted from a proper orthogonal decomposition (POD) analysis [see *Escauriaza*, 2008].

[53] The three-dimensional development of scour around the cylinder can be observed by plotting the evolution of the bed in time, which is defined by the grid nodes of the computational domain that conform the bed surface and provide the boundary conditions for the flow field solution. Figure 8 shows instantaneous snapshots of the bed at the same four instants in time reported in the description of the scouring process at the symmetry plane (t = 5, 40, 95, and 735 s). This sequence provides a global overview of the bed evolution, from which we can appreciate the complex dynamics of erosion in the vicinity of the cylinder. Two distinct phenomena are observed in different regions of the bed: (1) in the area surrounding the cylinder the bed is continuously scoured and the bed elevation decreases smoothly, except in the region closer to the symmetry plane where the bed elevation oscillates quasiperiodically, as demonstrated in the previous section, due to the generation of "sediment waves," which are clearly observed in all four images of Figure 8; and (2) in the region occupied by the legs of the THV at the sides of the cylinder, the bed dynamics is characterized by the emergence of a series of ripples, which will be described and studied in the next section.

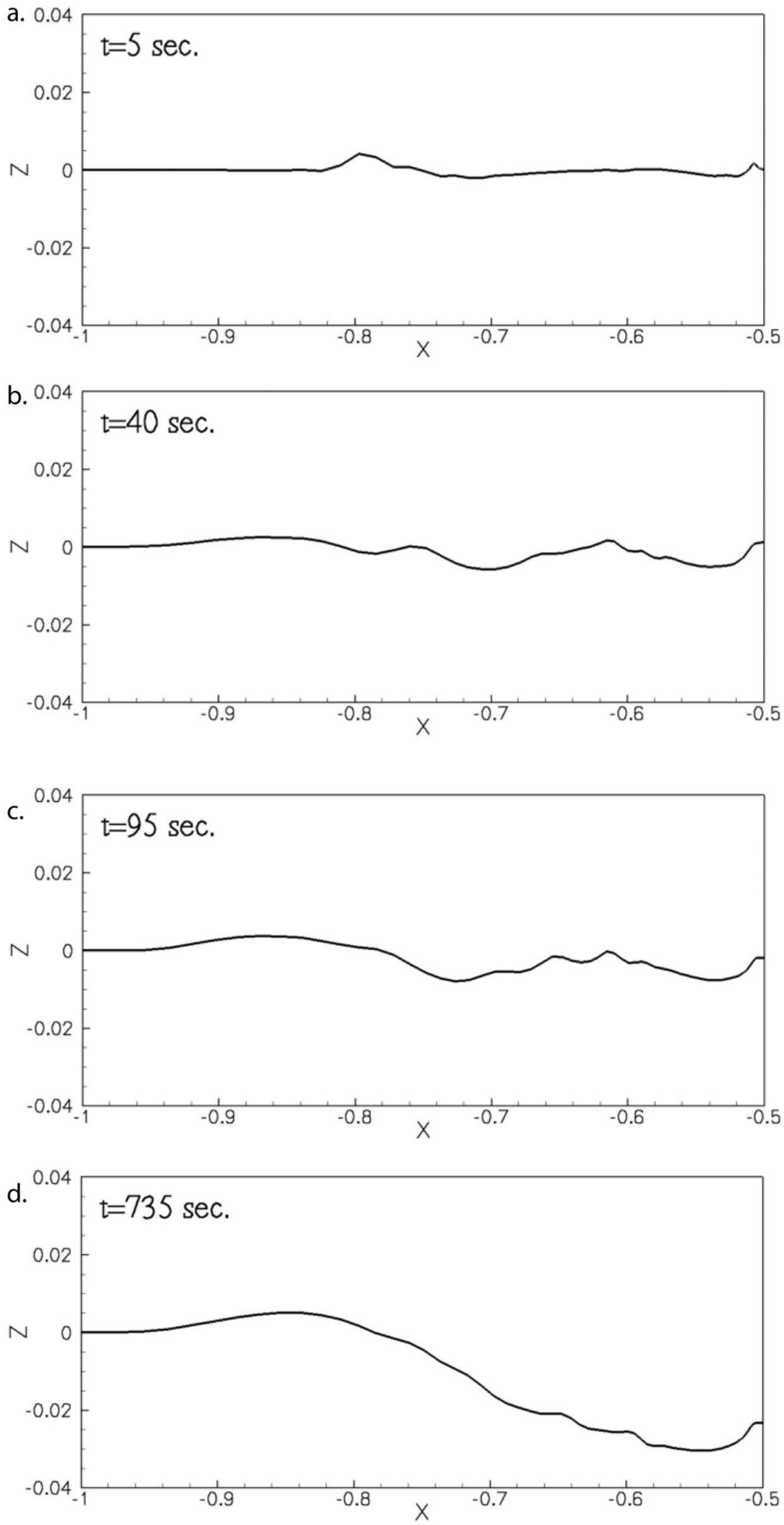

Figure 5. (a-d) Evolution of scour at the symmetry plane shows the same characteristics reported in the experiments. Two depressions become a single scour hole in front of the cylinder. Lengths are nondimensionalized with the cylinder diameter D, and the cylinder leading edge is located at $X = -0.5$.

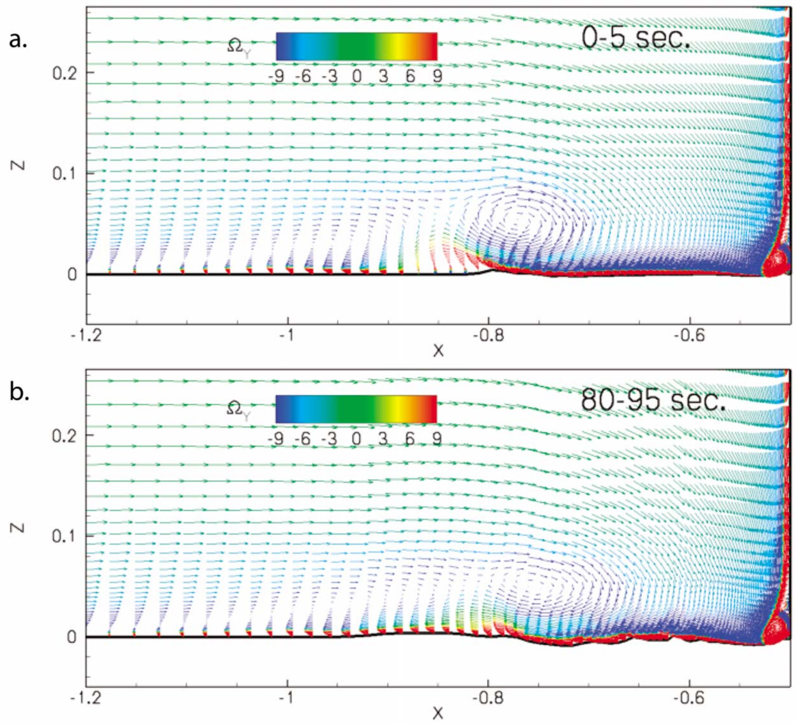

Figure 6. Averaged nondimensional velocity vectors colored by spanwise vorticity. (a) Time average for 0–5 s. (b) Time average for 80–95 s. Lengths are nondimensionalized with the cylinder diameter D, and the cylinder leading edge is located at $X = -0.5$.

[54] The apparent success of our model to capture for the first time dynamically rich features of the erosion process should be attributed, at least in part, to the fact that the DES model we employ captures all the essential dynamics of the THV system. URANS models typically do not provide detailed information on the evolution of erosion, or overpredict its initial stages [e.g., *Roulund et al.*, 2005].

[55] In this work we are able to provide for the first time information on the dynamic evolution of the bed. The instantaneous bed contours around the cylinder plotted in Figure 9 show the progression of erosion with the dynamic features already discussed. Note that Figures 9a–9d have different scales in order to show the adequate contour levels for the description of each stage of the scour process. In Figure 9a we can observe that the bed erosion is initiated at the base of the cylinder and near the symmetry plane in front of the cylinder. As a typical case of clear-water scour, the erosion only occurs in the region of the bed where the THV is located. After the first 5 s the first indications of the emergence of bed forms appear at the cylinder sides. Figures 9b and 9c show similar features, with the continuous development of bed forms and the maximum scour occurring always at approximately ±45° from the symmetry plane. Figure 9d shows a more advanced state of scour with larger bed structures, and a single scour hole around the cylinder. The sediment accumulation at around $X = -0.9$ can be clearly seen in front of the cylinder, and no scour takes place upstream of $X = -1.0$.

[56] All these results demonstrate that in addition to capturing the characteristics of the scour time series at the symmetry plane, the model can also represent the spatial features of the bed around the cylinder observed by *Dargahi* [1990], from the location of maximum scour to the remarkable dynamics of bed forms.

[57] Even though the scour process depicted in Figures 8 and 9 has all the qualitative characteristics observed in the experiments for the same Reynolds number, the rate at which the bed is eroded seen on the time series of maximum scour

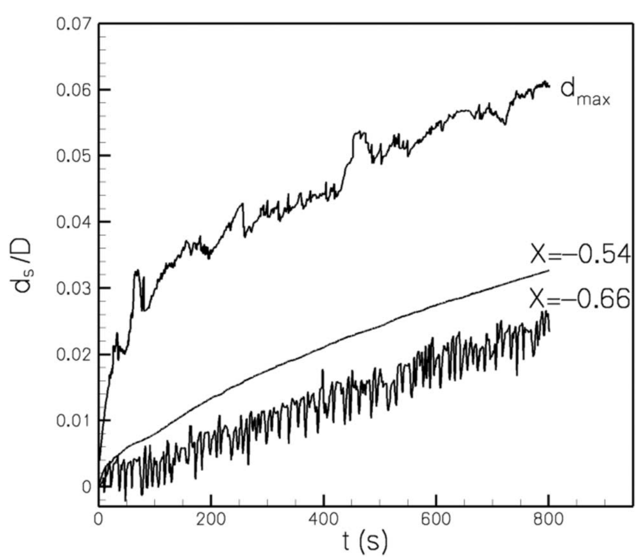

Figure 7. Maximum erosion on the bed and scour depths at two different points on the symmetry plane upstream of the cylinder.

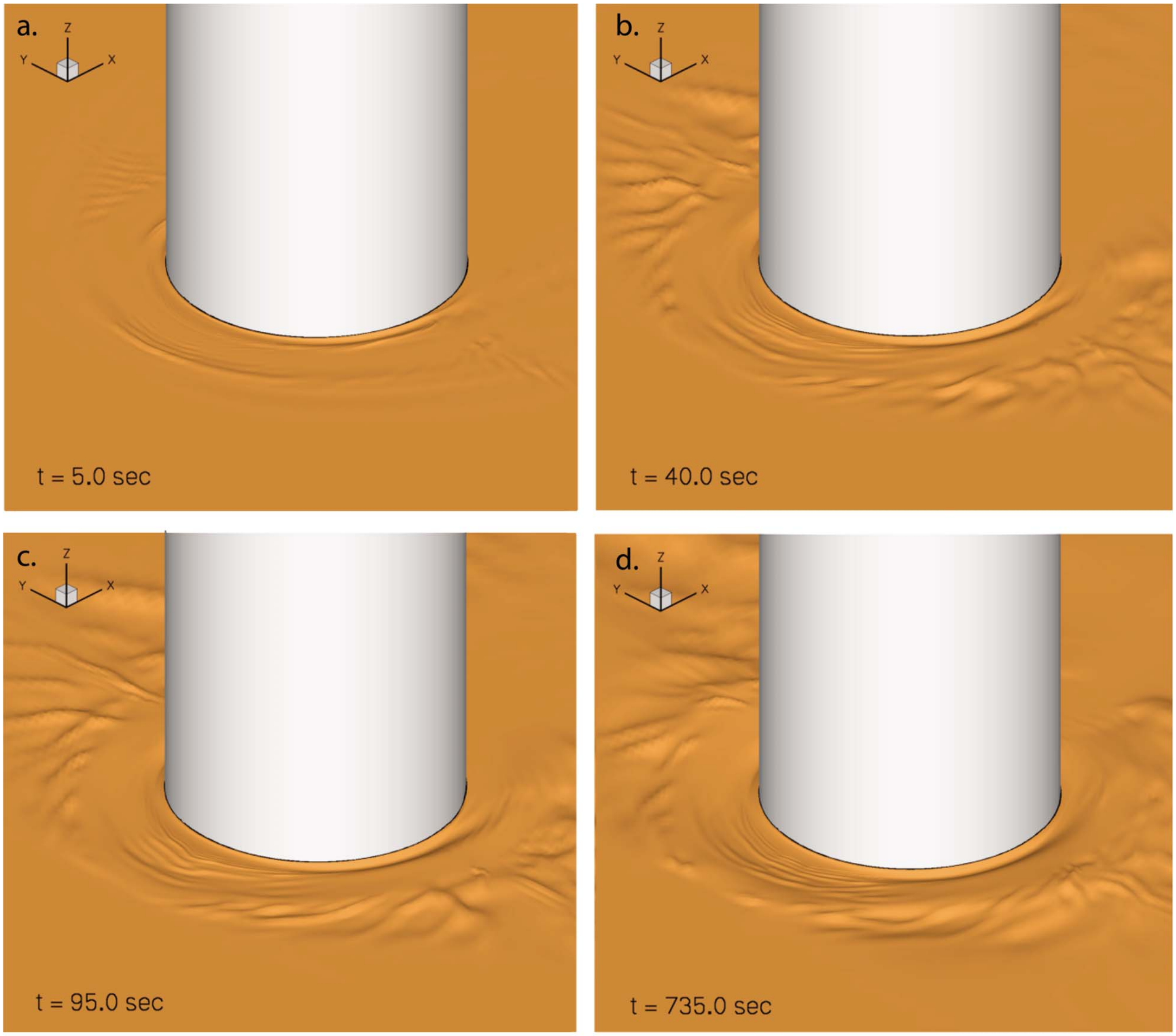

Figure 8. (a-d) Three-dimensional instantaneous images of the bed elevation, showing the evolution of the scour hole and the development of ripples around the cylinder.

on Figure 7 turns out to be slower than the experimental measurements. At 735 s, the deepest scour computed is approximately 0.9 cm ($d_s \approx 0.06$), while *Dargahi* [1990] reports a maximum erosion of 3 cm. The differences are likely due to previously discussed empirical formula used to calculate the bed areal concentration, which has been derived and calibrated with mean flow quantities. It is also important to recognize that unlike previous studies, which employed significant calibration of the constants of various formulas to match the experimental data, in this work no such calibration was attempted. The main reason for this is that given the lack of a physically based model that links the instantaneous fluctuations of hydrodynamic forces with the bed areal concentration any calibration attempt of an existing time-averaged model is futile and bound to be case specific. Additionally, the sudden avalanche of material in regions of steep slopes is not an instantaneous phenomenon, and it can also dislodge and drag a large mass of sediment. It is also important to note that the simulations were performed assuming a constant inflow velocity profile, while the mobile bed experiments had an initial flow transient before reaching the steady state at Re = 39,000. These quantitative discrepancies not withstanding, the model captures the process of bed form formation along the legs of the THV, which was also reported by *Dargahi* [1990] (see the following section).

[58] The flow field in the vicinity of the cylinder is modified as scour progresses, but the THV system maintains the same overall characteristics reported for the flat bed case (see the comments by *Dargahi* [1990]) with two large persistent vortices that are shed quasiperiodically from the separation point. Instantaneous snapshots of spanwise vorticity at the symmetry plane, depicted in Figure 10, give a clear idea of the flow dynamics during the scour process.

[59] The initial accumulation of sediment at the bed after the first 5 s, shown in Figure 10a, is located exactly in the region of

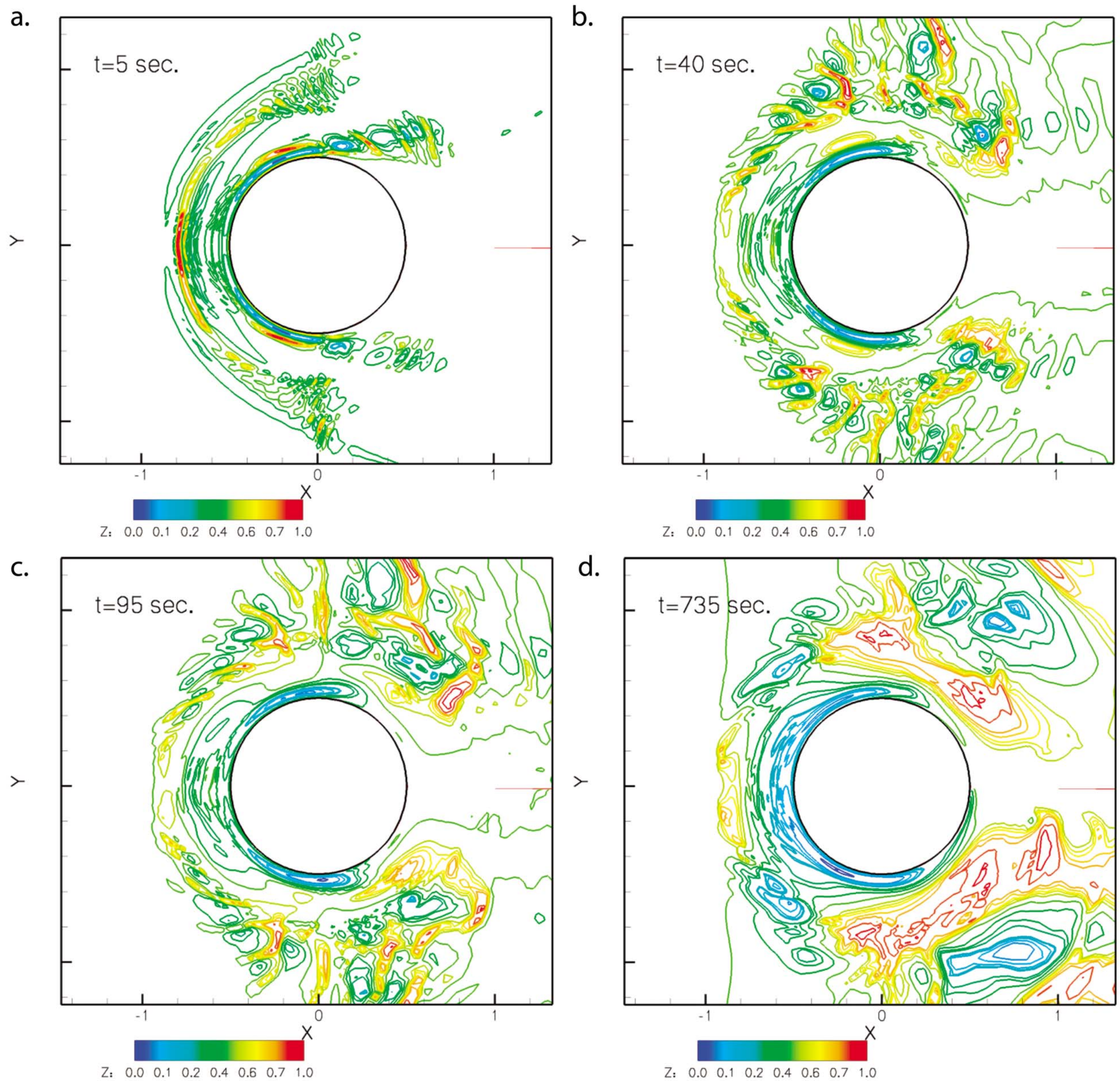

Figure 9. (a-d) Contours of bed elevation at four instants in time. The range of contours changes as scour progresses to give additional details of the instantaneous bed features in the vicinity of the cylinder. Lengths are nondimensionalized with the cylinder diameter D, and the cylinder leading edge is located at $X = -0.5$.

the symmetry plane where the first destabilization of the vortex takes place. During the entire simulation period we observe that the vortical structures that experience the instability and continuous interplay between the backflow and zero-flow modes are always situated inside the scoured region. Analysis of the bed scour and the flow show that the shear stress increment that occurs due to the emergence of the zero-flow mode of the THV system is the primary mechanism that initiates scour at the bed. This can also be concluded from the finite-time averaged flow fields that were shown in Figure 6.

[60] It is important to note that the separation region from which the new vortices emerge does not experience a significant bed deformation as seen in Figure 10b for $t = 735$ s. The instability of the THV, which is also responsible for the ejections of wall fluid and the disorganization of the vortex closer to the cylinder, is sustained throughout the simulation time and has the largest influence on the bed load flux close to the cylinder that produces the periodic variations observed in some areas of the bed. Figure 10b also coincides with an instant that corresponds to the activation of the zero-flow mode, which starts exactly at the position where the scour hole begins at the symmetry plane. This is also the position of the outer turn observed for the finite-time averaged structures in Figure 6.

[61] The shear stress distribution is modified by the scoured bed as shown in Figure 11, decreasing the original shear velocity magnitude in the front, and producing significant changes at the cylinder sides. The irregular distribution

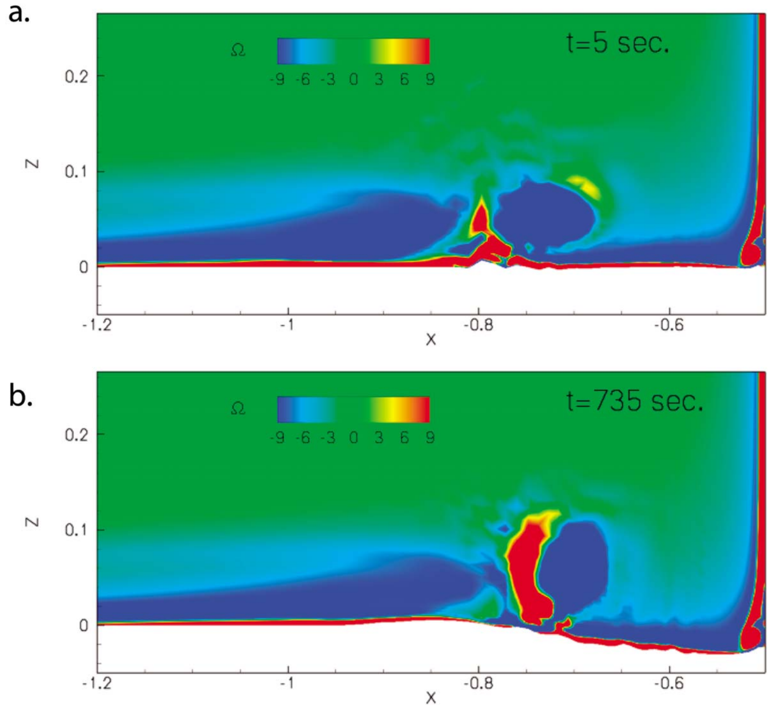

Figure 10. Instantaneous nondimensional spanwise vorticity at the symmetry plane: (a) at 5 s and (b) 735 s after the simulation started. Lengths are nondimensionalized with the cylinder diameter D, and the cylinder leading edge is located at $X = -0.5$. Velocities are nondimensionalized with the bulk velocity of the channel flow $\mathcal{U} = 0.26$ m/s.

of shear stress at the sides of the cylinder is connected to the bed form dynamics, since the upstream face of the ripples becomes an area of concentrated shear stress, inducing erosion and displacing the bed forms downstream. During the initial stages of scour, as seen in Figure 11 (top), the shear stress distribution has similar features to the flat bed case, except for the growth of the bed form instability at the cylinder sides, near the inner leg of the THV system. The intense fluctuations of the THV system generate the initial bed scour at the leading edge of the cylinder, up to approximately $X = -0.72$. The contours at 735 s in Figure 11 (bottom), on the other hand, show a decrease of the shear stress in front of the cylinder and a change on the distribution produced by the bed forms. The alternation of high and low zones of shear stress is displaced further away from the cylinder, along the most external part of the THV legs, and they are consistent with the larger amplitude and wavelength of the ripples in time (see Figure 8). Another important characteristic is the shear stress distribution at the cylinder sides. As scour progresses, it is evident in Figure 11 (bottom) that the zone of high shear starts wrapping around the cylinder in the downstream region.

4.2. Bed Form Dynamics

[62] As it was pointed out in the previous section, the simulations results show that the model reproduces the formation of ripples along the legs of the THV system, which were also observed in the experiments performed by *Dargahi* [1990]. In the present section we summarize the characteristics of bed forms as documented in previous field and laboratory experiments, and study the statistics of bed elevation at the sides of the cylinder.

[63] To evaluate the characteristics of the ripples in the flow, we compare our results with the information provided by *Dargahi* [1990], and compute statistics of the topography to see if they have the same properties of real bed forms measured in experiments or in the field. Ripples and bed forms in general have also been studied by performing statistical analysis of time series of bed elevation. Spectral analysis of the topography in experimental and field data has revealed power law relations of the spatial spectrum, with a −3 exponent of the wave number ($\sim\kappa^{-3}$), and frequency spectra with exponents f^{-2} and f^{-3} for high and low frequencies, respectively (for additional information the reader is referred to *Hino* [1968], *Jain and Kennedy* [1974], and *Nikora et al.* [1997]). Additional statistics were computed by *Jerolmack and Mohrig* [2005] to study bed forms from field data and numerical simulations. The bed topography was characterized by the root-mean-square (RMS) of bed elevation for different length scales defined by a spatial window of variable size. From the analysis of the bed fluctuations the spatial dependence of bed forms was shown to have a scale-invariant regime identified by a power law relation of the RMS statistic. The power law showed to be valid within the range of length scales where the internal dynamics is predominant as seen in real bed forms.

[64] In our numerical simulation, the interaction of the bed with the near-wall vortices produces the bed instability that

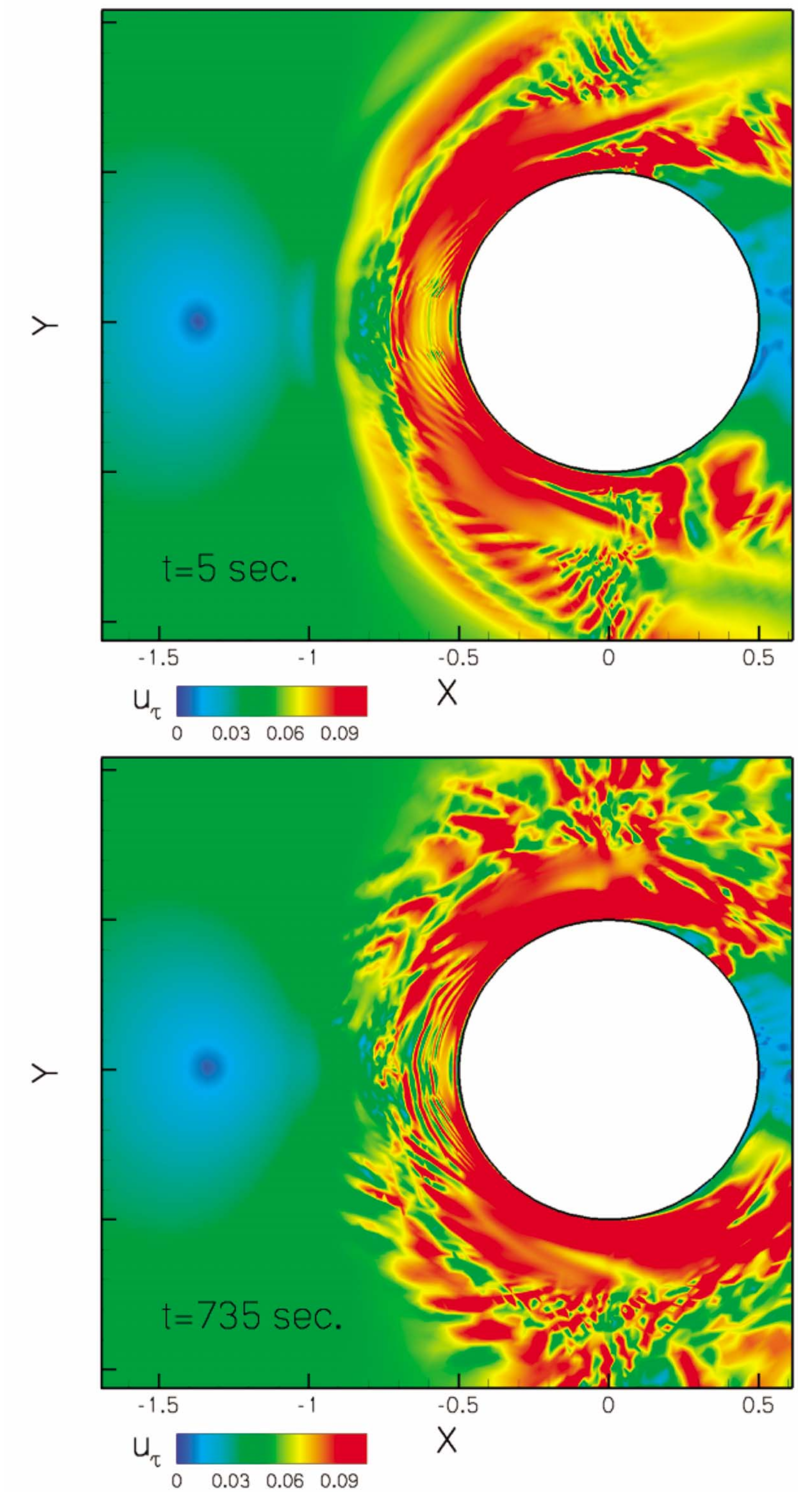

Figure 11. Instantaneous nondimensional shear velocity distribution at the bed during scour development. Zones of higher shear stress arise upstream of the ripples: (top) 5 s and (bottom) 735 s after the simulation started. Lengths are nondimensionalized with the cylinder diameter D, and the cylinder leading edge is located at $X = -0.5$. Velocities are nondimensionalized with the bulk velocity of the channel flow $\mathcal{U} = 0.26$ m/s.

gives rise to a series of ripples that grow and propagate downstream as observed in the sequence plotted in Figure 8. These bed forms, which appear typically in beds with fine sand as previously discussed, are formed at the THV location and have an oblique orientation with respect to the channel flow. The ripples later become perpendicular to the flow as they travel and merge in the downstream direction forming larger structures that shape the bed around the

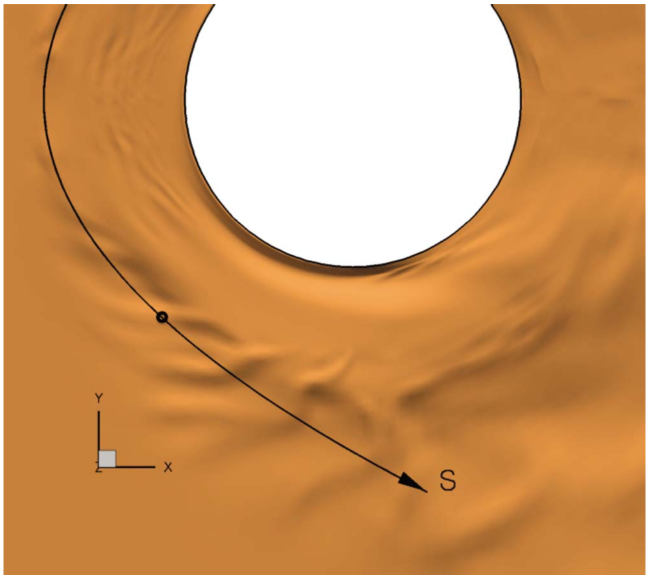

Figure 12. Definition of an arbitrary coordinate S across the centerline of the ripples, to simplify the analysis of bed elevation at the sides of the cylinder.

cylinder. The bed forms and the development of the scour hole produced by the THV have also a significant influence on the near-bed flow, and change the distribution of turbulent stresses at the bed (see Figure 11).

[65] *Dargahi* [1990] reported the bed forms as an important characteristic of the bed that was present during the entire experiment. In the description of the scour process, he commented that "[a]fter 5 seconds, scouring at the sides of the cylinder starts and additional sediment is transported by the arms of the horseshoe vortex system. The scouring causes small ripples to form at the sides of the cylinder. The ripples continuously migrate downstream with a speed of 0.1 m/s."

[66] The bed forms in our numerical simulation arise spontaneously at around 5 s after the scour flow starts, as reported for the experiments (see Figure 8a). The model does not require the implementation of specific boundary conditions that impose a perturbation intended to trigger the bed instability [see, e.g., *Roulund et al.*, 2005], as in the present simulation the instability is naturally excited by the resolved flow field past the surface-mounted obstacle. The ripples develop initially as oscillations of the bed elevation with small amplitude and short wavelength as observed experimentally in fine sand beds by *Coleman and Melville* [1996], but change continuously as they evolve in time and space. A particular characteristic observed in the scour evolution plots of Figure 8, is that the multiple small ripples generated initially (also called sand-wavelets by *Coleman and Melville* [1996]) start growing and merging, creating bed forms with different wave speeds as it will be subsequently shown. The development of the initial instability produce ripples with highly variable celerities, which determine a rapid initial merging that stabilizes as time progresses. It is important to note that these ripples generated by the THV exhibit smaller wavelengths and larger celerities compared to bed forms produced by the action of a turbulent boundary layer on a plane bed. The celerity of the ripples is approximately 38% of the bulk velocity of the flow, and their velocities are also similar in magnitude to the velocity computed for individual grains in the Lagrangian model of *Escauriaza and Sotiropoulos* [2011b].

[67] Linear stability analyses have been utilized to determine the growth of perturbations at the interface between the bed and the flow [*Kennedy*, 1969; *Engelund and Fredsøe*, 1982]. In this particular case, however, multiple factors intervene on the generation ripples that occur only within a delimited area of the bed due to the action of the three-dimensional instantaneous near-bed flow induced by the quasiperiodic increments of the bed stresses driven by the dynamics along the legs of the THV system. The legs of the THV system consist of a series of streamwise helical vortices with predominant sweep-like events [*Escauriaza and Sotiropoulos*, 2011a], which set up an ideal condition for the initial development of ripples as pointed out by *Best* [1992].

[68] To verify that the results of the model can realistically capture the development of bed forms, we analyze statistically the bed elevation at the sides of the cylinder in space and time, to compare with the characteristics observed in real bed form dynamics, such as the observations of *Jerolmack and Mohrig* [2005]. Since the ripples are present only in a delimited area of the bed we study the dynamics of the topography along a vertical plane crossing their centerline, which coincides with the legs of the THV system as shown in Figure 12 in the definition of the coordinate S. Both sides of the cylinder provide statistically indistinguishable characteristics, thus the results presented herein correspond to the bed forms generated at the left face of the cylinder facing the flow.

[69] To characterize the complex processes that occur at the bed, we perform a statistical analysis of time series of topography along the S coordinate to compare with the known features of ripples in real conditions and determine if their statistics are consistent with experimental observations. In particular we study the statistics of bed elevation observed in bed forms in fine sand, such as the spectrum of ripples measured by *Hino* [1968] and *Nikora et al.* [1997] and the scaling analysis performed by *Jerolmack and Mohrig* [2005] in field and simulated data of bed topography.

[70] Figure 13a shows contours of bed elevation that illustrate the bed form evolution in time and space. From the topography contours, we can identify the appearance of structures of different sizes, and multiple merging episodes that occur at the sides of the cylinder (see Figure 13b). The bed forms are generated periodically near the symmetry plane (S = 0), but their characteristics differ from the ripple generation in plane-bed conditions that generally travel at consistently decreasing speeds [*Coleman and Melville*, 1994]. In this case, the initial velocity of the ripples is not too high, since the shear stress in this zone is high and controlled by the low-frequency bimodal dynamics of the horseshoe vortex (see Figures 3 and 11), and the velocity of the near-bed flow is small compared to the velocity at the sides of the cylinder. As the bed forms move to higher velocity regions they speed up, but merging events and formation of larger ripples slow down the migration of these structures downstream. This phenomenon gives the characteristic shape of the structures observed in Figure 13.

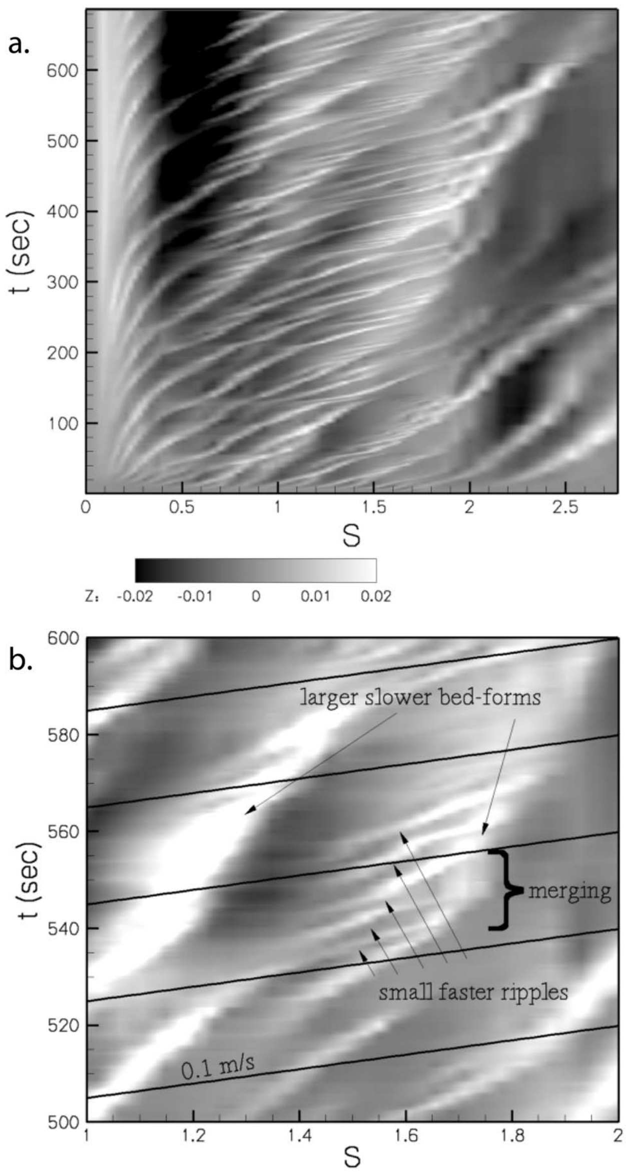

Figure 13. (a) Contours of bed elevation in time along the S coordinate show the propagation of ripples at the sides of the cylinder. (b) Magnification of the map shows that the bed form celerity for small ripples is similar to the experimental result of 0.1 m/s reported by *Dargahi* [1990] and represented by the black lines.

[71] Details of the bed form dynamics are observed in the magnified map in Figure 13b. The ripple celerity is relatively similar to the experimental measurements of 0.1 m/s for small bed forms reported by *Dargahi* [1990]. Large ripples that are formed by merging, however, travel slowly and become more persistent in time.

[72] We perform a statistical analysis of the ripples along the prescribed coordinate to study the length-scale dependence of bed fluctuations. We evaluate the RMS of the calculated bed elevation, as a function of the length scale along S. As discussed by *Jerolmack and Mohrig* [2005], the size distribution of bed forms exhibits a power law relationship of the RMS with the length scale. We define a spatial window Δs, and compute the RMS of bed elevation for each scale, obtaining a distribution of the statistic in equation (14) as a function of Δs, which is denoted by $b'_{\Delta s}$:

$$b'_{\Delta s} = \left\langle b^2_{\Delta s} \right\rangle^{1/2} \approx \left[\frac{1}{N} \sum_{i=1}^{N} \left(b_i - \bar{b} \right)^2 \right]^{1/2} \tag{14}$$

where b_i is the bed elevation, $\bar{b}$ is the average along S, and N is the total number of data points if the bed is sampled along the prescribed S coordinate at intervals of size Δs.

[73] The scale invariance of the spatial fluctuations generated by the bed forms determines an increase in magnitude with the length scale of the statistic defined in equation (14). This relation is similar to the definition of the roughness exponent on the RMS diagram of *Barabási and Stanley* [1995], such that

$$\Im_{\Delta s} = \sqrt{\Delta s}\, b'_{\Delta s} \sim (\Delta s)^{\vartheta} \tag{15}$$

where Δs is the corresponding length scale, and $\Im_{\Delta s}$ identifies the variation of the bed root-mean-square with Δs.

[74] This is the same technique employed by *Chrisohoides and Sotiropoulos* [2003] to determine the time scale of Lagrangian coherent structures in free-surface turbulent flows from flow visualization experiments. For their case the fluctuation diagrams constructed from time series of light intensity were shown to saturate at the coherence scale of the vortical structures [see also *Keeling et al.*, 1997].

[75] The scale at which $\Im_{\Delta s}$ deviates from the power law relation in Figure 14a represents the approximate maximum distance where the spatial correlation of the bed forms is maintained [*Barabási and Stanley*, 1995]. The height fluctuations of the bed are spread in space and $\Delta s \approx 0.3$ is the characteristic length below which they remain correlated. This length scale coincides with the largest wavelengths of ripples in the simulated domain.

[76] This specific analysis is different to the statistics studied by *Nikora and Hicks* [1997], since they vary the total length of the studied profile in which the standard deviation is computed. Here we built the fluctuation diagram in Figure 14a by sampling the total length along the prescribed S coordinate at intervals of size Δs (see *Keeling et al.* [1997] and *Chrisohoides and Sotiropoulos* [2003] for details). The RMS magnitude gives information of the bed roughness, and the slope of the power law in the log-log diagram depicted in Figure 14a specifies the spatial dependence structure of the bed forms. In this particular case we see that the RMS of bed elevation maintains a relatively constant value throughout time for different scales as $\Im_{\Delta s} \sim \Delta s^{0.5}$ indicating the self-similar characteristics of the bed until the coherence or correlation length scale is reached. It is important to point out that *Dargahi* [1990] did not report the maximum length of the bed forms. Our model however reproduces the exact time at which the bed destabilizes, and the velocity of propagation of the bed forms compared to the experimental observations.

[77] The spatial standard deviation along S is plotted in time in Figure 14b. Since bed forms cannot grow indefinitely, it is also expected to reach a steady state consistent

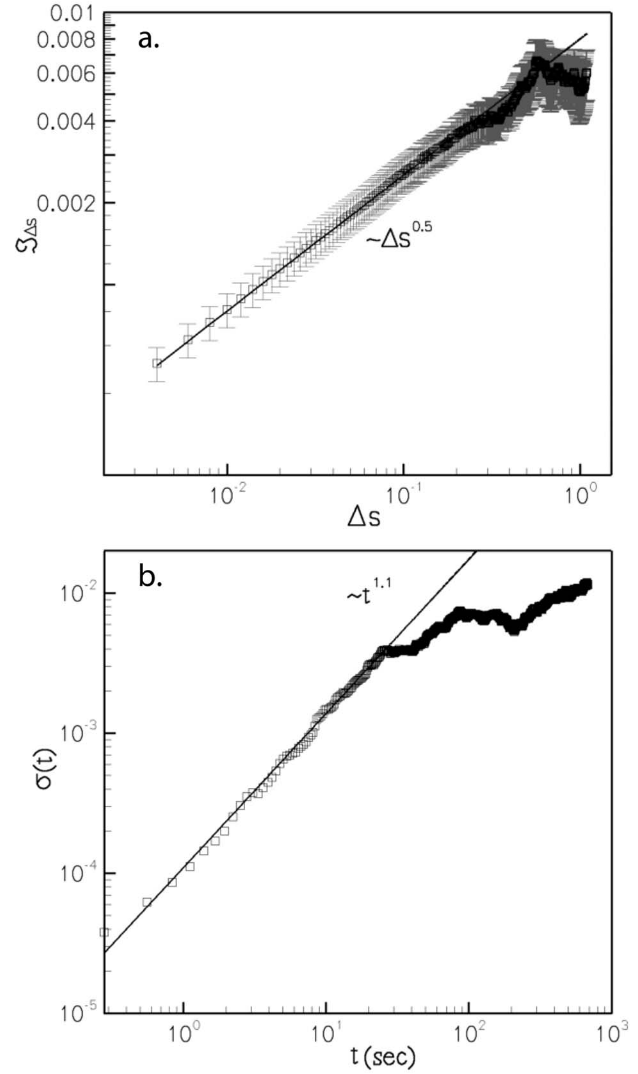

Figure 14. Statistics of bed elevation at the cylinder side. (a) Fluctuation diagram averaged over time; the error bars correspond to the standard deviation of $\Im_{\Delta s}$. (b) Evolution of the standard deviation of the bed elevation in time. For the initial development of ripples, the standard deviation along S has a power law relation.

with the continuous generation of bed forms at a statistically converged wavelength and amplitude. The break on the power law relationship determines an approximate time scale of 27 s for the regime change on the standard deviation growth. This plot also indicates that during the first 27 s the bed rapidly evolves from the flat bed condition to a regime with self-similar bed forms traveling downstream in a periodic manner (see comments of the autocorrelation function and spectrum below). The slower evolution of the standard deviation in time after this initial period explains the approximately constant slope of 0.5 in the fluctuation diagram shown in Figure 14a.

[78] Additional information can also be obtained from a temporal analysis of bed elevation time series. All points along the prescribed coordinate show the same dynamics in time and frequency domains. As an example, the time periodicity of the bed at a point along the coordinate S is observed on the autocorrelation plot of Figure 15a. The oscillations produced by the passing of "sand-waves" can be computed to compare the statistical properties of the ripples at the cylinder sides with results from experimental observations of bed forms [*Hino*, 1968; *Nikora et al.*, 1997]. Figure 15b shows the frequency spectrum of bed elevation for the same point on the bed along the S coordinate. For at least an order of magnitude, the spectrum coincides with the −2 power law relation reported for ripples. Using experimental data, *Hino* [1968] showed that the frequency spectrum of bed forms has a power law relation with a decay of f^{-2} for low frequencies near the peak of the spectrum, and argued that the −2 power law was mainly associated to the dynamics of ripples. *Nikora et al.* [1997] showed the same −2 slope of the spectrum, for a similar range of

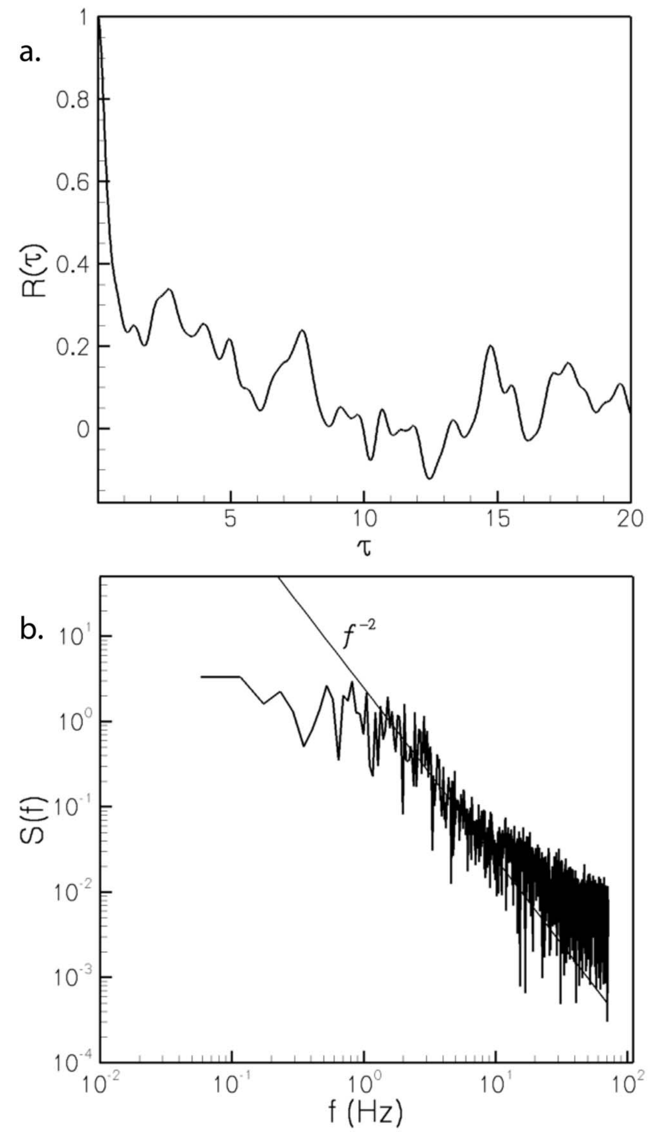

Figure 15. (a) Autocorrelation and (b) frequency spectrum of bed elevations time series on the bed, at the point $X = -0.354$ and $Y = -0.678$, which corresponds to the point marked along coordinate S in Figure 12.

frequencies in series of bed elevations of actual rivers. The model cannot maintain the −2 spectrum at high frequencies since the solution of the Exner equation (12) is based on a dissipative scheme for the derivatives, which in absence of a subgrid model for fluctuations of the bed elevation, it might smooth excessively high-frequency features of the bed elevation. Detailed analysis of the frequency spectrum of Figure 15b, and along this entire transect of the bed, shows several commensurate dominant frequencies: f = 0.1166, 0.2915, 0.5830, and 0.8162 Hz. The rational ratio among these frequencies reveals that the dynamics of the bed forms is periodic. This values are similar to the lower frequencies observed in the THV, whose dynamics produce the large sweep events that trigger the initiation of bed forms at the sides of the obstacle.

[79] It is important to note that the bed forms in the vicinity of the cylinder are well represented by the numerical model and the domain discretization. In the vertical direction for the entire computational domain and at the cylinder boundary, the grid resolution is fine enough as it contains 9 layers of grid nodes for a distance equal to the particle diameter [*Escauriaza and Sotiropoulos*, 2011b]. Further away from the cylinder the length of the bed forms might be related to the grid resolution. If the grid is too coarse, the model can no longer capture bed forms of small sizes as they might become smaller than the finest grid size. The work carried out in this investigation shows that a relatively simple sediment transport model that uses the resolved flow obtained with DES can capture the rich dynamics of erosion and bed form development. Future work will focus on investigating the SGS contributions and a more complete modeling approach to improve the description of the small-scale ripples and their effects on the dynamic evolution of the bed [*Coleman and Nikora*, 2009].

5. Conclusions and Future Work

[80] The unsteady bed load and erosion model developed in this research can reproduce qualitatively all the features for the initial stages of scour in the vicinity of a surface-mounted cylinder, which are a consequence of the direct influence that the large-scale coherent structures of the THV system have on erosion and deposition in fine sediment beds under clear-water scour conditions.

[81] The bed load model is based on a novel unsteady momentum equation of sediment grains along with well-known empirical formulas of areal concentration and solves the Exner equation simultaneously with the unsteady flow equations. This approach improves the degree of description of the bed load transport flux and defines a modeling framework to build general fully coupled models of turbulent flows in complex geometries with sediment transport and bed erosion for realistic conditions. The results of the simulations elucidate the three-dimensional evolution of the bed topography by the action of the unsteady turbulent horseshoe vortex induced by the presence of the cylinder. The model reproduces most of the characteristics observed by *Dargahi* [1990] during the initial scour around the cylinder, including the shape of the bed at the symmetry plane as time progresses, the bed oscillations connected to the vortex shedding of the THV system, and the development of ripples at the cylinder sides along the legs of the vortex.

[82] An important discrepancy between simulations and experimental observations is with regard to the computed time rate of scour, which is slower than observed. The reasons for the slower scouring process should be attributed to the inherent modeling simplifications due to the lack of accurate expressions capable of representing some of the complex processes occurring at the interface between the sediment and the flow.

[83] The bed areal concentration only considers the instantaneous shear stress to determine the volume of particles per unit area that participate in transport. Even though the model can readily incorporate alternative formulations for estimating this quantity, it is clear that equilibrium formulas that rely on empirical considerations obtained for steady unidirectional flows are not adequate to simulate unsteady sediment transport with a dynamic nonequilibrium boundary condition of the erodible bed. Additional discrepancies may arise due to the initial adjustment of the flow to reach the steady state Reynolds number in the experimental flume. The simulations are performed with a constant inflow, since no information is given on the initial flow transient, thus the effects of the accelerating bulk flow on the evolution of the bed are not accounted for.

[84] The avalanche model [*Marieu et al.*, 2008] maintains instantaneously the correct bed slopes. The complex characteristics of real beds, with different particle sizes and internal distribution of stresses, can produce temporal and spatial variabilities on the avalanche flux magnitudes, and set in motion a large number of particles when the bed slope exceeds the maximum angle of repose. A fully descriptive model of the local avalanches of material might be incorporated in the future to determine precisely the total mass of sediment that participates on the sliding events.

[85] An important contribution of our work is to underscore the need for careful experimental and computational studies of particle entrainment and concentration distribution in nonequilibrium unsteady conditions. The actual areal concentration of particles, γ, used in the present research depends on multiple interactions and feedbacks between the bed and the unsteady flow. The recent erosion experiments around a sidewall-mounted block in a rectangular channel performed by *Radice et al.* [2008], have shown for the first time the complex time and spatial distribution of sediment areal concentration in nonequilibrium unsteady bed load transport processes produced by the large-scale coherent structures of the flow.

[86] Numerical simulations with the model developed in this research can help to design laboratory experiments, which will give the high-resolution data needed to improve the predictive capabilities of the model. Ideally, detailed experiments should be performed to study the stress-strain relations of the active layer of the bed. These high-resolution data at the bed can give the necessary information to determine the initial mass and velocity of the sediment that is dislodged, depending on the local properties of the sediment and the instantaneous stresses produced by the local flow velocity and pressure fields.

[87] High-resolution experiments tracking individual particles in turbulent flows with large-scale coherent structures can help to determine the entrainment probabilities, with the

purpose of developing stochastic approaches for sediment entrainment and parameterize the inherent uncertainties that may arise due to the variability of grain sizes and bed packing. Experiments could also be oriented toward studying the local avalanche events produced by the failure of the bed in nonequilibrium unsteady conditions. To represent correctly these phenomena on the bed model, however, we would need to parameterize the avalanche flux to determine the actual mass that is dislodged, and the sediment velocities during the avalanche and its distribution and deposition of the grains.

[88] A fundamental aspect of the erosion model that also needs to be addressed is the effect of the smallest scales of motion and bed fluctuations smaller than the grid resolution. By ignoring the dynamics of the scales that are not resolved, we had to implement a numerical scheme that contained a predetermined dissipation which can affect the accuracy of the solution for the bed elevation at the resolved scales. The development of a dynamic subgrid scale parameterization will require detailed studies of the scale dependence to incorporate on the numerical solution the bed fluctuation effects up to the grain resolution, including the interaction between the smallest scales of the flow and the sediment particle dynamics. Recent models developed for landscape evolution [*Passalacqua et al.*, 2006] could provide the starting point for such undertaking.

[89] The modeling limitations notwithstanding, the present model can capture the emergence and development of bed forms. The ripples exhibit a celerity comparable to the experimental observations, and the complete statistical analysis performed on the series of bed elevation showed that their dynamics was consistent with the features observed for real bed forms in experiments and in the field. The ripples at the sides of the cylinder, however, exhibit a shorter wavelength compared with bed forms produced by the turbulent boundary layer in unidirectional flows. Based on our previous simulations for the flat, rigid bed [*Escauriaza and Sotiropoulos*, 2011a], we observe that the spatial structure of the near-bed flow at the start of scour does not appear to contain wavelengths and/or patterns that could force the specific bed form dynamics that emerge in the mobile bed simulation. In another paper [*Escauriaza and Sotiropoulos*, 2011a] we reported the mean limiting streamlines on the bed around the cylinder, which do not contain any apparent footprints of the bed forms that emerge when the bed is allowed to move. Therefore, we can conclude with reasonable certainty that it is the coupled interaction of the energetic THV with the mobile bed that gives rise to the simulated bed forms at the cylinder sides.

[90] To the best of our knowledge, the present model is the first to successfully simulate the dynamics of the initial stages of erosion by unsteady near-bed coherent structures, and the first to capture the development of bed forms with a fully three-dimensional simulation of the flow field coupled with a general Exner equation, using only first principles in the physical derivation of the bed model, and solved in a time-accurate manner. In this context it is important to highlight the work of *Giri and Shimizu* [2006] and *Shimizu et al.* [2009] in the development of a 2-D URANS model coupled with a stochastic sediment transport and a morphodynamic model to simulate dune migration and stage-discharge relationships in a channel [*Giri and Shimizu*, 2007]. In addition, the recent investigation carried out by *Chou and Fringer* [2010] could simulate the interaction of the near-bed flow and the formation and evolution of ripples in a domain with periodic boundaries using a 3-D LES model coupled with the Exner equation.

[91] Extensive studies should be carried out in the future to explore the variation of the statistical parameters with respect to the flow dynamics and sediment properties. These investigations will likely require to implement a more detailed description of the sediment dynamics for denser flows with interparticle collisions. The flexibility of the model developed in this research will allow the inclusion of particle-flow and particle-particle momentum interactions, incorporating collisions and turbulence modulation in flows with higher concentrations, along with subgrid scale models of turbulent dispersion that consider the unresolved scales of turbulence motion.

[92] The unsteady transport model and the bed model can also be utilized as a general framework for more complex sediment transport formulations. Additional progress can be made by considering other effects on the governing equations to simulate flows with higher concentrations. General problems of sediment transport in natural rivers and streams with mobile beds and bed load and suspended transport might require a two-fluid approach for a full Eulerian formulation [*Drew*, 1983], or a parcel representation in which a volume in space represents a fixed number of actual particles [*Loth*, 2000]. These approaches, however, require a careful description of the particle stresses and of the relations between sediment and the unresolved turbulence field in the context of the hybrid turbulence models or LES.

[93] To develop a model capable of capturing the full extent of the complexity of the sediment transport processes and bed evolution, the solution of the momentum and mass conservation within the active layer of the bed would need to be considered. The recent volumetric momentum balance proposed by *Coleman and Nikora* [2008, 2009] gives a consistent framework from which this complex model can be derived to determine the particle entrainment using instantaneous quantities. This extension for the present model would be ideally suited to investigate the dynamics of bed forms and their relation with the flow, and also incorporate a realistic description of the local avalanches that occur in situations with steep bed slopes.

[94] **Acknowledgments.** This work was supported by NSF grants EAR-0120914 (as part of the National Center for Earth-Surface Dynamics) and EAR-0738726. C.E. has also been supported by Fondecyt grant 11080032. Computational resources were provided by the University of Minnesota Supercomputing Institute.

References

Ahn, H. T., and Y. Kallinderis (2006), Strongly coupled flow/structure interactions with a geometrically conservative ALE scheme on general hybrid meshes, *J. Comput. Phys.*, *219*, 671–696.

Allen, J. R. L. (1966), On bed forms and palaeocurrents, *Sedimentology*, *6*, 153–190.

Ancey, C., T. Böhm, M. Jodeau, and P. Frey (2006), Statistical description of sediment transport experiments, *Phys. Rev. E*, *74*, 011302.

Anderson, T. B., and R. Jackson (1967), A fluid mechanical description of fluidized beds, *Ind. Eng. Chem. Fundam.*, *6*, 527–539.

Aris, R. (1962), *Vectors, Tensors, and the Basic Equations of Fluid Mechanics*, Prentice Hall, Englewood Cliffs, N. J.

Auton, T. R., J. C. R. Hunt, and M. Prud'homme (1988), The force exerted on a body in inviscid unsteady non-uniform rotational flow, *J. Fluid Mech.*, *197*, 241–257.

Barabási, A. L., and H. E. Stanley (1995), *Fractal Concepts in Surface Growth*, Cambridge Univ. Press, New York.

Best, J. (1992), On the entrainment of sediment and initiation of bed defects: insights from recent developments within turbulent boundary layer research, *Sedimentology*, *39*, 797–811.

Chou, Y.-J., and O. B. Fringer (2010), A model for the simulation of coupled flow-bed form evolution in turbulent flows, *J. Geophys. Res.*, *115*, C10041, doi:10.1029/2010JC006103.

Chrisohoides, A., and F. Sotiropoulos (2003), Experimental visualization of lagrangian coherent structures in aperiodic flows, *Phys. Fluids*, *15*, L25–L28.

Coleman, S. E., and B. W. Melville (1994), Bed-form development, *J. Hydraul. Eng.*, *120*, 544–560.

Coleman, S. E., and B. W. Melville (1996), Initiation of bed forms on a flat sand bed, *J. Hydraul. Eng.*, *122*, 301–310.

Coleman, S. E., and V. I. Nikora (2008), A unifying framework for particle entrainment, *Water Resour. Res.*, *44*, W04415, doi:10.1029/2007WR006363.

Coleman, S. E., and V. I. Nikora (2009), Exner equation: A continuum approximation of a discrete granular system, *Water Resour. Res.*, *45*, W09421, doi:10.1029/2008WR007604.

Crowe, C. T., M. Sommerfeld, and Y. Tsuji (1998), *Multiphase Flows With Droplets and Particles*, CRC Press, Boca Raton, Fla.

Dargahi, B. (1989), The turbulent flow field around a circular cylinder, *Exp. Fluids*, *8*, 1–12.

Dargahi, B. (1990), Controlling mechanism of local scour, *J. Hydraul. Eng.*, *116*, 1197–1214.

Devenport, W. J., and R. L. Simpson (1990), Time-dependent and time-averaged turbulence structure near the nose of a wing-body junction, *J. Fluid Mech.*, *210*, 23–55.

Doligalski, T. L., C. R. Smith, and J. D. A. Walker (1994), Vortex interactions with walls, *Annu. Rev. Fluid Mech.*, *26*, 573–616.

Drew, D. A. (1983), Mathematical modeling of two-phase flow, *Annu. Rev. Fluid Mech.*, *15*, 261–291.

Engelund, F., and J. Fredsøe (1976), A sediment transport model for straight alluvial channels, *Nordic Hydrol.*, *7*, 293–306.

Engelund, F., and J. Fredsøe (1982), Sediment ripples and dunes, *Ann. Rev. Fluid Mech.*, *14*, 13–37.

Engelund, F., and E. Hansen (1967), *A Monograph on Sediment Transport to Alluvial Streams*, Tek. Vorlag, Copenhagen.

Escauriaza, C. (2008), Three-dimensional unsteady modeling of clear-water scour in the vicinity of hydraulic structures: Lagrangian and Eulerian perspectives, Ph.D. thesis, Univ. of Minn., Minneapolis, Minn.

Escauriaza, C., and F. Sotiropoulos (2009), Trapping and sedimentation of inertial particles in three-dimensional flows in a cylindrical container with exactly counter-rotating lids, *J. Fluid Mech.*, *641*, 169–193.

Escauriaza, C., and F. Sotiropoulos (2011a), Reynolds number effects on the coherent dynamics of the turbulent horseshoe vortex system, *Flow Turbul. Combust.*, *86*, 231–262.

Escauriaza, C., and F. Sotiropoulos (2011b), Lagrangian model of bed-load transport in turbulent junction flows, *J. Fluid Mech.*, *666*, 36–76.

Exner, F. M. (1920), Zur physik der dünen, *Anz. Akad. Wiss. Wien Math. Naturwiss. Kl.*, *129*, 929–952.

Exner, F. M. (1925), Über die wechselwirkung zwischen wasser und geschiebe in flüssen, *Anz. Akad. Wiss. Wien Math. Naturwiss. Kl.*, *134*, 165–204.

Giri, S., and Y. Shimizu (2006), Numerical computation of sand dune migration with free surface flow, *Water Resour. Res.*, *42*, W10422, doi:10.1029/2005WR004588.

Giri, S., and Y. Shimizu (2007), Validation of a numerical model for flow and bedform dynamics, *Annu. J. Hydraul. Eng. Jpn. Soc. Civ. Eng.*, *51*, 139–144.

Hino, M. (1968), Equilibrium-range spectra of sand waves formed by flowing water, *J. Fluid Mech.*, *34*, 565–573.

Hirt, C. W., A. A. Amsden, and J. L. Cook (1974), An arbitrary Lagrangian-Eulerian computing method for all flow speeds, *J. Comput. Phys.*, *14*, 227–253.

Hsu, T. J., J. T. Jenkins, and P. L. F. Liu (2004), On two-phase sediment transport: Sheet flow of massive particles, *Proc. R. Soc. London, Ser. A*, *460*, 2223–2250.

Hunt, J. C. R., A. A. Wray, and P. Moin (1988), Eddies, stream, and convergence zones in turbulent flows, in *Proceedings of the 1998 Summer Program*, pp. 193–208, Cent. for Turbul. Res., Stanford, Calif.

Jain, S. C., and J. F. Kennedy (1974), The spectral evolution of sedimentary bed forms, *J. Fluid Mech.*, *63*, 301–314.

Jerolmack, D. J., and D. Mohrig (2005), A unified model for subaqueous bed form dynamics, *Water Resour. Res.*, *41*, W12421, doi:10.1029/2005WR004329.

Kaftori, D., G. Hetsroni, and S. Banerjee (1995), Particle behavior in the turbulent boundary layer: I. Motion, deposition, and entrainment, *Phys. Fluids*, *7*, 1095–1106.

Keeling, M. J., I. Mezić, R. J. Henry, J. McGlade, and D. A. Rand (1997), Characteristic length scales of spatial models in ecology via fluctuation analysis, *Proc. R. Soc. London, Ser. B*, *352*, 1589–1601.

Kennedy, J. F. (1969), The formation of sediment ripples, dunes, and antidunes, *Annu. Rev. Fluid Mech.*, *1*, 147–168.

Kirkil, G., G. Constantinescu, and R. Ettema (2008), Coherent structures in the flow field around a circular cylinder with scour hole, *J. Hydraul. Eng.*, *134*, 572–587.

Kovacs, A., and G. Parker (1994), A new vectorial bedload formulation and its application to the time evolution of straight river channels, *J. Fluid Mech.*, *267*, 153–183.

Lakehal, D. (2002), On the modelling of multiphase turbulent flows for environmental and hydrodynamic applications, *Int. J. Multiphase Flow*, *28*, 823–863.

Loth, E. (2000), Numerical approaches for motion of dispersed particles, droplets, and bubbles, *Prog. Energy Combust. Sci.*, *26*, 161–223.

Marieu, V., P. Bonneton, D. L. Foster, and F. Ardhuin (2008), Modeling of vortex ripple morphodynamics, *J. Geophys. Res.*, *113*, C09007, doi:10.1029/2007JC004659.

McElroy, B., and D. Mohrig (2009), Nature of deformation of sandy bed forms, *J. Geophys. Res.*, *114*, F00A04, doi:10.1029/2008JF001220.

Nelson, J. M., R. L. Shreve, S. R. McLean, and T. G. Drake (1995), Role of near-bed turbulence structure in bed load transport and bed form mechanics, *Water Resour. Res.*, *31*, 2071–2086.

Nikora, V. I., and D. M. Hicks (1997), Scaling relationships for sand wave development in unidirectional flow, *J. Hydraul. Eng.*, *123*, 1152–1156.

Nikora, V. I., A. N. Sukhodolov, and P. M. Rowinski (1997), Statistical sand wave dynamics in one-directional water flows, *J. Fluid Mech.*, *351*, 17–39.

Nikora, V. I., I. McEwan, S. McLean, S. Coleman, D. Pokrajac, and R. Walters (2007), Double-averaging concept for rough-bed open-channel and overland flows: Theoretical background, *J. Hydraul. Eng.*, *133*, 873–883.

Niño, Y., A. Atala, M. Barahona, and D. Aracena (2002), Discrete particle model for analyzing bedform development, *J. Hydraul. Eng.*, *128*, 381–389.

Paik, J., C. Escauriaza, and F. Sotiropoulos (2007), On the bimodal dynamics of the turbulent horseshoe vortex system in a wing-body junction, *Phys. Fluids*, *19*, 045107.

Paik, J., F. Sotiropoulos, and F. Porté-Agel (2009), Detached eddy simulation of the flow around two wall-mounted cubes in tandem, *Int. J. Heat Fluid Flow*, *30*, 286–305.

Paola, C., and V. R. Voller (2005), A generalized Exner equation for sediment mass balance, *J. Geophys. Res.*, *110*, F04014, doi:10.1029/2004JF000274.

Parker, G., G. Seminara, and G. Solari (2003), Bedload at low shields stress on arbitrarily sloping beds: Alternative entrainment formulation, *Water Resour. Res.*, *39*(7), 1183, doi:10.1029/2001WR001253.

Passalacqua, P., F. Porté-Agel, E. Foufoula-Georgiou, and C. Paola (2006), Application of dynamic subgrid-scale concepts from large-eddy simulation to modeling landscape evolution, *Water Resour. Res.*, *42*, W06D11, doi:10.1029/2006WR004879.

Radice, A., S. Malavasi, and F. Ballio (2008), Sediment kinematics in abutment scour, *J. Hydraul. Eng.*, *134*, 146–156.

Raudkivi, A. J. (1997), Ripples on stream bed, *J. Hydraul. Eng.*, *123*, 58–64.

Roulund, A., B. M. Sumer, J. Fredsøe, and J. Michelsen (2005), Numerical and experimental investigation of flow and scour around a circular pile, *J. Fluid Mech.*, *534*, 351–401.

Shimizu, Y., S. Giri, S. Yamaguchi, and J. Nelson (2009), Numerical simulation of dune-flat bed transition and stage-discharge relationship with hysteresis effect, *Water Resour. Res.*, *45*, W04429, doi:10.1029/2008WR006830.

Simpson, R. L. (2001), Junction flows, *Annu. Rev. Fluid Mech.*, *33*, 415–443.

Spalart, P. R. (2009), Detached-eddy simulation, *Annu. Rev. Fluid Mech.*, *41*, 181–202.

Spalart, P. R., and S. R. Allmaras (1994), A one-equation turbulence model for aerodynamic flows, *Rech. Aerosp.*, *1*, 5–21.

Spalart, P. R., W. H. Jou, M. Strelets, and S. R. Allmaras (1997), Comments on the feasibility of LES for wings and on a hybrid RANS/LES

approach, in *Advances in DNS/LES*, edited by C. Liu and Z. Liu, Greyden Press, Columbus, Ohio.
Ushijima, S. (1996), Arbitrary Lagrangian-Eulerian numerical prediction for local scour caused by turbulent flows, *J. Comput. Phys.*, *125*, 71–82.
van Rijn, L. C. (1984), Sediment transport, part I: Bed load transport, *J. Hydraul. Eng.*, *108*, 1215–1218.
Venditti, J. G., M. A. Church, and S. J. Bennett (2005), Bed form initiation from a flat sand bed, *J. Geophys. Res.*, *110*, F01009, doi:10.1029/2004JF000149.
Venditti, J. G., M. A. Church, and S. J. Bennett (2006), On interfacial instability as a cause of transverse subcritical bed forms, *Water Resour. Res.*, *42*, W07423, doi:10.1029/2005WR004346.

C. Escauriaza, Departamento de Ingeniería Hidráulica y Ambiental, Pontificia Universidad Católica de Chile, Av. Vicuña Mackenna 4860, Santiago 7820436, Chile. (cescauri@ing.puc.cl)

F. Sotiropoulos, St. Anthony Falls Laboratory, Department of Civil Engineering, University of Minnesota, Minneapolis, MN 55414, USA. (fotis@umn.edu)